Browse all Theses and Dissertations

Theses and Dissertations

2017

An Experimental Investigation of Residual Stress Development during Selective Laser Melting of Ti-6Al-4V

Nathan Charles Levkulich
Wright State University

An Experimental Investigation of Residual Stress Development during Selective Laser Melting of Ti-6Al-4V

A thesis submitted in partial fulfillment
of the requirements for the degree of
Master of Science in Materials Science and Engineering

By

NATHAN CHARLES LEVKULICH
B.S.M.E, Wright State University, 2016

2017
Wright State University

WRIGHT STATE UNIVERSITY

GRADUATE SCHOOL

December 4, 2017

I HEREBY RECOMMEND THAT THE THESIS PREPARED UNDER MY SUPERVISION BY <u>Nathan Charles Levkulich</u> ENTITLED <u>An Experimental Investigation of Residual Stress Development during Selective Laser Melting of Ti-6Al-4V</u> BE ACCEPTED IN PARTIAL FULLFILLMENT OF THE REQUIREMENT FOR DEGREE OF <u>Master of Science in Materials Science and Engineering</u>.

_____
Nathan Klingbeil, Ph.D.
Thesis Director

_____
Joseph C. Slater, Ph.D., P.E.
Chair, Department of Mechanical and Materials Engineering

Committee on Final Examination:

_____
Nathan Klingbeil, Ph.D.

_____
Joy Gockel, Ph.D.

_____
Sheldon L. Semiatin, Ph.D.

_____
Barry Milligan, Ph.D.
Interim Dean of the Graduate School

ABSTRACT

Levkulich, Nathan Charles. M.S.M.S.E. Department of Mechanical and Materials Engineering, Wright State University, 2017. An Experimental Investigation of Residual Stress Development during Selective Laser Melting of Ti-6Al-4V.

Selective laser melting (SLM) is an additive manufacturing (AM) process that gives rise to large thermal gradients and rapid cooling rates that lead to the development of undesirable residual stress and distortion. In this work, a number of different techniques (i.e., x-ray-diffraction, hole-drilling, layer-removal, and contour) were utilized to establish the effect of process parameters on residual-stress development during SLM of Ti-6Al-4V. The measurements indicated that higher laser power, slower scan speed, smaller stripe width, reduced substrate overhang, and reduced build plan area each reduce the level of residual stress. In addition, the correlation between microstructure, crystallographic texture, and residual stress were investigated using electron backscatter diffraction (EBSD) and backscatter electron (BSE) imaging. The experimental results from this work provide a quantitative foundation for future simulations of residual stress evolution during SLM and provide an informed understanding of residual stress development that can be used for process planning and improvement.

TABLE OF CONTENTS

vi

List of Figures

List of Tables

ACKNOWLEDGMENTS

First, I would like to thank my Wright State thesis committee members Dr. Nathan Klingbeil and Dr. Joy Gockel for investing countless hours into my thesis work. Both Dr. G and Dr. K have given me great insight for my thesis work and have created a great research environment at Wright State University. In addition, I would also like to thank John Middendorf, Adrian Dewald, Joey Walker, Luke Sheridan, Kaitlin Kollins, Kate Wertz, Travis Brown, and Rick Reibel for their large contributions to my work.

Next, I would like to thank my mother, father, and family for their love and support throughout my college years. My mother has been my biggest encourager and supporter, while my father has taught me to be a hard worker and a disciple of Christ.

Finally, I would like to thank Dr. Sheldon L. Semiatin. I truly have enjoyed getting to know "Lee" on a personal level and as a research scientist. Lee is perhaps the most intelligent person I have ever met. However, Lee's two traits that I admire the most are his humbleness and his willingness to help others. He has invested several years into my development as a person and scientist and I cannot thank him enough for everything he has done for me. I have enjoyed our many conversations and jokes along the way and I look forward to continue working with him. I will always consider Lee to be a part of my family.

1. INTRODUCTION

Additive manufacturing (AM), a process that has been evolving for decades, is a layer by layer addition process that fabricates 3D components and is controlled by computer software. AM enables a reduction in post processing waste, geometric friendliness, and a reduction in sub-assemblies. Typically, conventional manufacturing components involve rolling, forging, and extrusions that often require several assemblies and post processing. Thus, the cost of conventional manufactured components increases with complexity. Because of this, the AM process has gained interest as a viable cost effective option for customized biomedical components (e.g. tissues, implants, scaffold structures), and for reducing the buy to fly ratio and lead time in aerospace components [1-3].

Specifically, titanium and nickel-based alloys are commonly used materials for high temperature aerospace applications. One of the most commonly used aerospace metals is Ti-6Al-4V because it offers a high strength to weight ratio and good corrosion properties. Ti64 is a two phase alloy at room temperature and has microstructure and mechanical properties that are reliant on prior thermal history. Because of the popularity of conventionally manufactured Ti64 and the need for lighter and stronger aerospace components, work has been undertaken to evaluate the potential of AM Ti64 for future aerospace applications. Previous work in AM of Ti64 has primarily focused on evaluating the effect of process parameters on porosity, microstructure evolution, and

mechanical properties [1, 4-9].

Selective laser melting (SLM), a commonly used metal AM process, has the capability to fabricate fully dense metal components with high resolution and internal passages. The SLM process employs a laser beam as its heat source and fuses powder particles together one layer thickness at a time in order to fabricate 3D components. One disadvantage of the SLM process is that large thermal gradients and fast cooling rates occur during the fabrication process and typically lead to the development of residual stress. In AM, residual stress is undesirable and often leads to component distortion and thermal cracking that ultimately results in build failure. However, limited work exists on assessing the evolution of residual stress during SLM. Therefore, this thesis is an experimental investigation to establish methods to control, reduce, and correctly measure residual stress in the SLM of Ti-6Al-4V.

1.2 Additive Manufacturing Processes

AM technologies offer an exciting outlook for a variety of new and innovative applications that until now have been unachievable. In this regard, AM is a low energy process that greatly reduces material waste by up to 90% (compared to conventional manufacturing) and eliminates the need for multiple fabrication steps. Because fewer fabrication steps are utilized, the component can reach the desired market more quickly [10]. Unlike traditional manufacturing, post processing is often not required and thus, AM fabricated components can be lighter and still maintain their functionality specifications [10]. Furthermore, the AM process enables almost unlimited customization for complex and novel

geometric components. However, several shortcomings of the AM process include process control, dimensional tolerance, and surface finish [10].

Throughout the past decade, the number of new and innovated AM processes has been increasing. However, only 7 AM processes are currently acknowledged by the International Organization for Standardization. Out of the seven accepted AM processes, material extrusion, vat polymerization, and material jetting are three processes that are utilized for polymer AM, while the two most popular metal AM processes are directed energy deposition (DED) and powder bed fusion (PBF). Both DED and PBF processes can fabricate fully dense metal components, yet their operating process parameter ranges are drastically different resulting in several advantages and disadvantages (Figure 1) [11]. Nevertheless, the methodology employed for each build fabrication is generally the same.
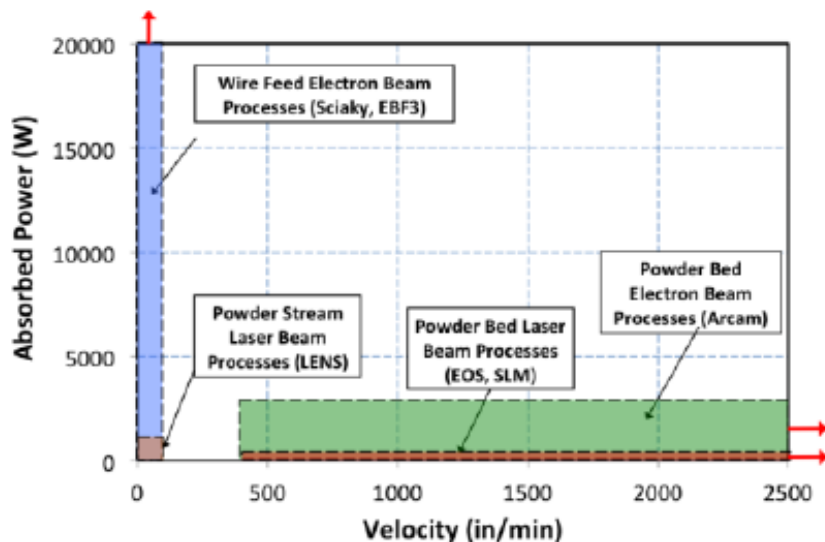
Figure 1: Different process parameter operating ranges of several different DED and PBF processes [11]

Typically, metal AM build fabrication is initiated by the component being modeled in a 3D software package. Next, the model is converted into a

3

STereoLithography (.STL) file containing readable 2D slices. The STL file is input into the AM system and process parameters that dictate build quality and fabrication rate are selected. The build process is mostly automated and rarely requires supervision. Once component fabrication is complete, the component is removed from the substrate and additional post processing may be required. Furthermore, the AM build fabrication process is shown in Figure 2.
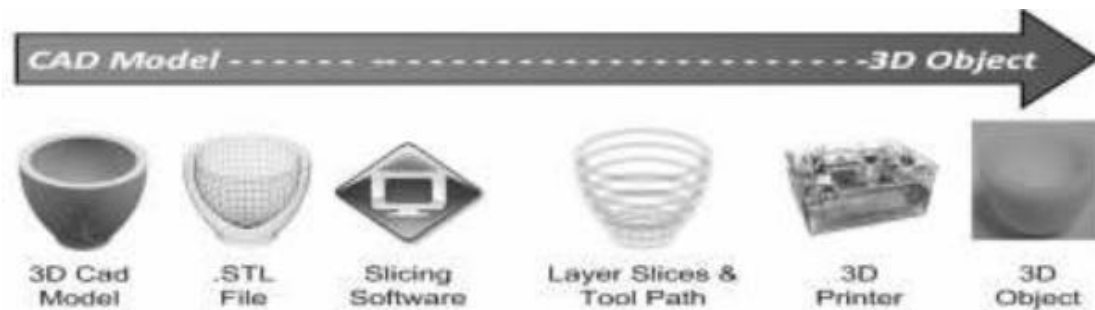
Figure 2: Build methodology utilized for each AM fabrication [12]

1.2.1 Directed Energy Deposition

As described in [13], DED metal processes are commonly used to manufacture large volume AM components with decent resolution and surface roughness (Figure 3). During DED fabrication, material in the form of powder or wire is fed into the processes melt pool, hence forming solidified material tracks. Each track is deposited adjacent to the previous deposited track and typical track thickness is greater than 100 microns. In order to produce fully dense layers and components, the melt pool employed during fabrication is 0.25-1 mm in diameter and penetrates 0.1-0.5 mm in depth. For each added layer, the scan direction is rotated to avoid preferential grain growth and increase anisotropy in the material. A visible afterglow occurs throughout the duration of the build process because of the large energy density inputted [14]. This allows the AM build to act as a

4

heat sink, hence reducing thermal gradients and the development of residual stress [14]. Additionally, larger layer thickness and melt pool size enables DED to have a faster fabrication rate than PBF even though scan speeds are much slower [14]. However, DED fabricates components with inferior surface roughness and dimensional accuracy.

Several examples of DED processes are Optomec's Laser Engineered Net Shaping (LENS), Direct Metal Deposition (DMD), and NASA Langley's Electron Beam Free Form Fabrication (EBF3). Powder fed DED processes such as Optomec's LENS, are advantageous for restoring damaged components [15]. As described in [13], material can be fed into the melt pool by three different methods: 4 nozzle feeding, coaxial feeding, or single feeding. Each feeding technique has several advantages and disadvantages. In addition, powder excess is a common occurrence during powder fed DED and because of this, steps must be taken to recycle the unused powder.

Wire DED processes, such as the NASA's EBF3, are effective in fabricating large simple geometries with low porosity [13]. By utilizing a wire as feed material, excess material waste is typically eliminated. Nevertheless, fabrication of complex geometric components with low porosity remains a continual challenge for this process.
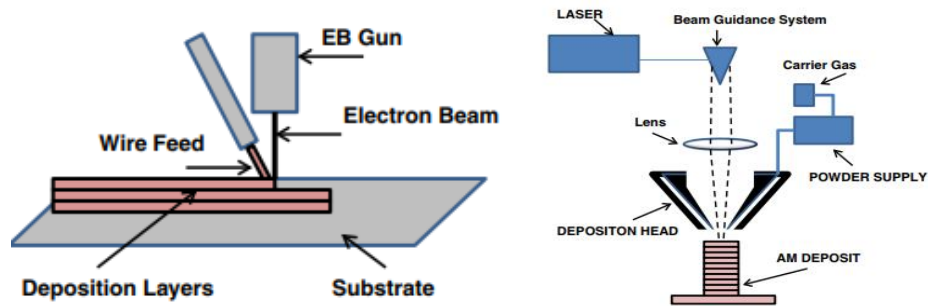
Figure 3: Overview of wire (left) and powder (right) DED processes [15]

1.2.2 Powder Bed Fusion

Unlike DED processes, the PBF process consists of a heat source, powder bed, and raking mechanism. Before the heat source is employed, the powder bed is raised one layer thickness, and powder is spread uniformly over the build region. Typical layer thickness for PBF is less than 100 microns which enables PBF to have better surface finish and better dimensional accuracy than DED. During PBF fabrication, a rotational scan strategy is implemented to increase material anisotropy and help reduce directional residual stress. Two of the most popular PBF processes are electron beam melting (EBM) and selective laser melting (SLM) (Figure 4).

As described in [14], EBM processes such as ARCAM, employ an electron beam as a heat source and use a two-step process for build fabrication. Powder is first spread one layer thickness and a low energy density scan is used to pre-sinter the entire powder bed surface. A second high energy density scan is utilized to melt the sintered powder and form fully dense layers. EBM typically has a faster production rate than PBF because electron beams can operate at higher scan speeds and higher powers than laser beams. This permits larger layer thicknesses and larger powder sizes to be utilized. Furthermore, the build

6

fabrication occurs in a vacuum environment causing contamination, such as, oxidation to be largely avoided. Lastly, EBM's unique ability to maintain a preheated powder bed greatly reduces thermal gradients and residual stresses throughout the build process [16].

Perhaps, the most dimensionally accurate metal AM process is SLM because a layer thickness of less than 50 microns is typically utilized. Similar to EBM, powder is spread over the build region one layer thickness at a time where several lenses and mirrors focus the heat source onto the powder bed. Next, the laser beam is employed fusing each freshly spread powder layer to the underlying material. Unlike EBM, the PBF process typically transpires in a gas atomized environment. Additionally, one of the largest drawbacks of SLM, is that the process induces large thermal gradients and fast cooling rates throughout the build process. This causes the evolution of residual stress to occur in large magnitudes.
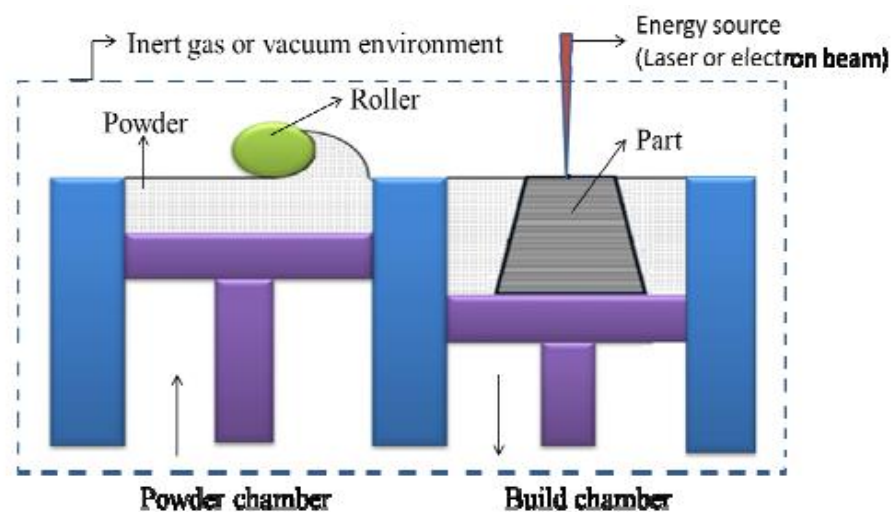
Figure 4: Overview of PBF process [17]

1.2.3 AM Process Parameters and Process Mapping

Each metal AM build is controlled by process parameters that are selected before each build and dictate density, material properties, and residual stress. Some important AM process parameters previously defined in literature are laser power, laser spot size, scan speed, layer thickness, powder shape, powder size, hatch spacing, dwell time, preheat temperatures, and scan strategy [1]. Energy density defined in Equation 1, takes into account several important process parameters and influences the shape and size of the processes' melt pool. In (1), P is the laser power, v is the scan speed, h is the hatch spacing, and t is the layer thickness. High energy densities induce a large melt pool area, while low energy densities will produce a small melt pool area. Additionally, the correct tailoring of energy density is a necessity and can lead to lack-of-fusion or keyholing defects if done incorrectly (Figure 5).

Keyholing defects often occur when the depth of the melt pool is greater than twice the width. Keyholing takes place at high energy densities and causes material to evaporate at the bottom of the melt pool creating circular porosity throughout the build. By contrast, lack of fusion porosity occurs when an insufficient amount of energy density is input into the added layer. Thus, the melt pool does not penetrate deep enough to fuse the added layer to the underlying material, which causes the formation of elongated porosity. Each defect negatively affects the integrity of the AM build by inducing undesirable porosity. Therefore, process parameters must be tailored correctly in order to achieve fully dense components.

$$E = \frac{P}{v * h * t} \tag{1}$$
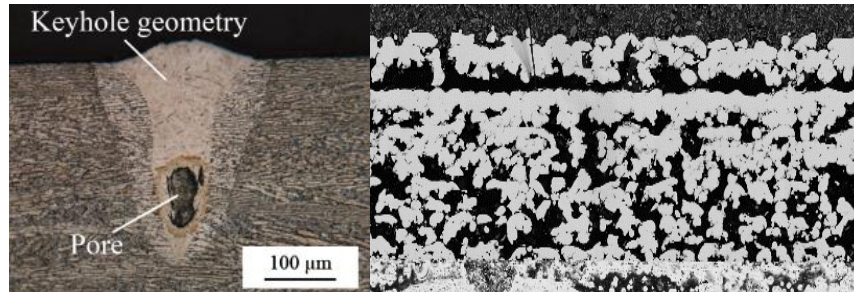
Figure 5: Key holing (left) and lack of fusion (right) AM defects [18]

In order to examine AM build quality (e.g. porosity, microstructure, and texture), standard metallography must be performed. Therefore, extensive amounts of time and cost must be undertaken to gain insight about the overall build quality. However, one modeling method developed to reduce the need for large experimental investigations is process mapping. Process mapping developed by Bueth et al. at Carnegie Melon, eliminates the need for time consuming and costly experimental investigation by modeling the effect of important process parameter (e.g. laser power, scan speed, material feed rate, component geometry, and temperature gradients) on melt pool geometry, cooling rates, residual stress, and microstructure evolution [19-24]. This modeling approach has gained popularity because it can be applied to a wide variety of materials and AM processes. In reference to the present work, some notable process mapping attempts have been done by Vasinonta et al [19], Bontha et al. [20], and Gockel et al [23]. The importance of each of these authors' work will be discussed in later sections. In addition, Ti64, IN625, and IN718 are several materials that have been applied to the process mapping approach [23, 11, 24].

1.3 Ti-6Al-4V

1.3.1 Overview

Ti64 is a two phase alloy at room temperature and is currently one of the most widely used titanium alloys. Ti64 exhibits excellent toughness, ductility, and corrosion properties that make it ideal for applications such as aircraft turbine disks, surgical implants, and pressure vessels [25]. At room temperature Ti64 consists of a hexagonal closed-packed α phase and a body center cubic β phase that are dependent on prior thermal history. The 6 atomic % of aluminum stabilizes the α phase, while the 4 atomic % of vanadium stabilizes the β phase. Compared to commercially pure titanium, the addition of aluminum and vanadium increases the β transus of the material to around 980°C. When Ti64 is heated above 980°C, the only phase present is the β phase, however, the α phase begins to nucleate and grows as the material is cooled below the β transus. The shape and size of the α phase is dictated by thermal history of the material.

The processing of titanium alloy ingots generally occurs in four stages [26]. In stage I, the material is homogenized in the β phase. Secondly, during stage II, the material is forged and rolled at temperatures above or below the β transus. During Stage III, a solution heat treatment is utilized to enable the formation of the desired microstructure. Lastly, an annealing heat treatment is sometimes implemented to remove residual stresses in the material. During the processing of Ti64, three α phase microstructure outcomes can occur: 1) lamellar 2) bimodal or duplex, and 3) fully equiaxed (Figure 7).

1.3.2 Ti-6Al-4V Microstructure

As described in [26-27], the lamellar/platelet microstructure occurs when the material is homogenized forged, rolled, and heat treated above the β transus. As the material is cooled below the β transus, the lamellar microstructure nucleates and grows within the previously formed β grains. Alpha laths can either form parallel to one another in colonies or cross each other in a basketweave configuration known as Widmanstätten microstructure. The size and orientation of the alpha grains is determined by the speed of the cooling rate. Faster cooling rates produce finer α lath, while slower cooling rates will produce thicker α lath. Furthermore, typical methods to cool Ti64 after being heat treated above the β transus include furnace cooling, air cooling, and water quenching.

Furnace cooling Ti-6Al-4V exhibits the slowest cooling rate of the three methods and produces a colony α lath structure, in which the alpha phase nucleates on the grain boundaries of each β phase [27]. The α-laths begin to grow towards the interior of each β grain during the duration of the cooling procedure [27]. As the α-laths grow, they replace the prior β grains, hence producing a fully laminar microstructure. Air cooling consists of the heat treated material being removed from its heat treatment source and slowly being cooled by the ambient air. This procedure has a higher cooling rate than furnace cooling, and has been documented to produce Widmanstätten microstructure with small amounts of β phase still prevalent [27]. Lastly, the material can be cooled by water quenching. In this process the material being heat treated is removed from the heat source and is directly placed in water. Out of the three cooling

11

processes water quenching has the highest cooling rate and produces a martensitic microstructure in Ti64 [27].
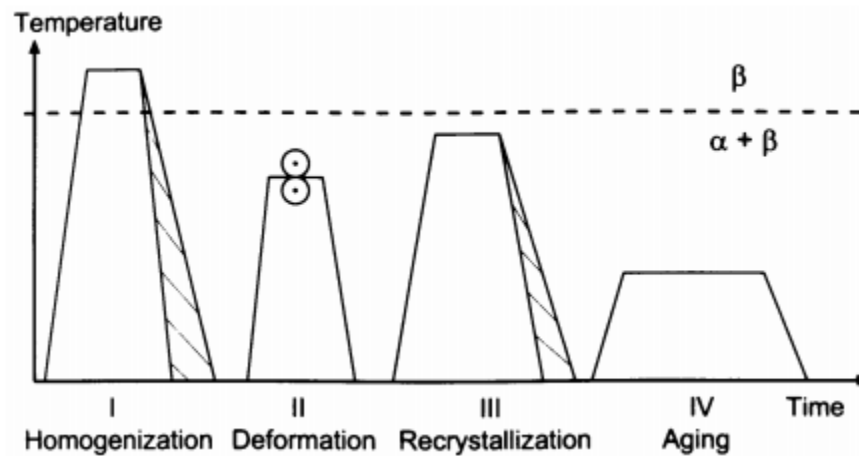
Figure 6: Processing procedures used to obtain bimodal microstructure [26]

The bimodal and fully equiax microstructures occur when the material is homogenized above the *β* transus. The deformation and solution treatment process occurs below the *β* transus. The bimodal microstructure contains two forms of *α* phase: equiaxed and platelet particles. The platelet particles form during stage II, and are replaced by the equiaxed alpha particle during stage III (Figure 6). Slower cooling rates enable the equiax particles to grow and reduces the volume fraction of platelet particles. In order to obtain a fully equiaxed microstructure, the cooling rate must be reduced further allowing a longer duration for equiaxed particles to grow.
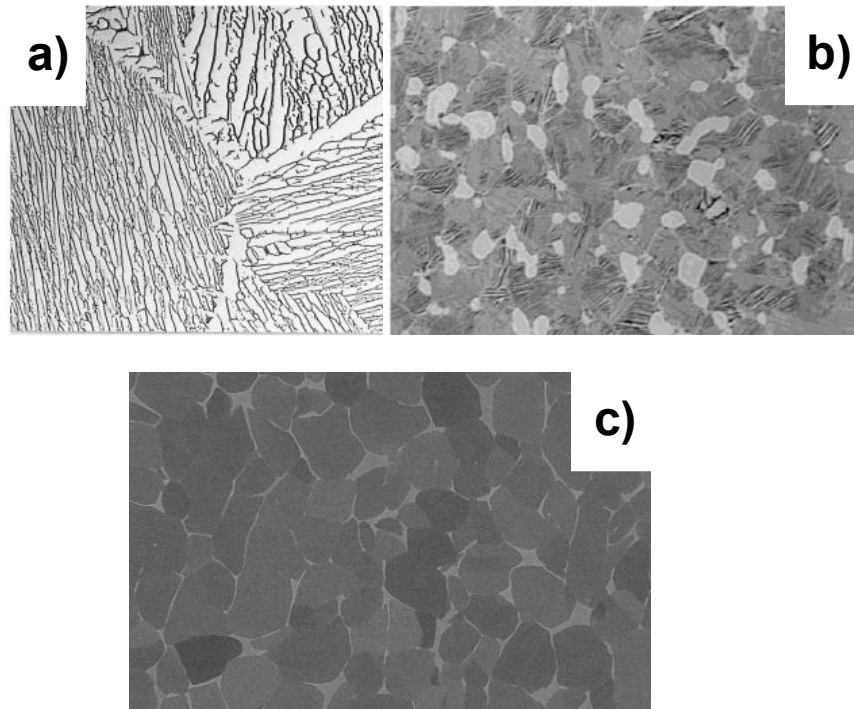
Figure 7: Micrographs of Ti64 α phase microstructures: lamellar (a), bimodal (b), and fully equiaxed (c) [26]

1.3.3 Crystallographic Texture

The development of crystallographic texture, commonly found in polycrystalline materials, represents the preferred orientation of the grains. In particular, titanium alloys are well known to develop crystallographic texture because of the low symmetry present in HCP crystal structures [28]. In this regard, crystallographic texture can be introduce into titanium alloys by the final deformation process of the material in Stage II, recrystallization of the material during Stage III, grain growth, or phase transformation [28,29]. During each of these scenarios, the grains in the material become strained and in order to maintain equilibrium, they plastically deform through several slip systems that alter the orientation of the grains. Thus, this process causes crystal lattice rotation to occur. Moreover, the understanding of texture in titanium alloys is critical because it can be used to predict prior thermo-mechanical history and can

have an effect on mechanical properties, such as fatigue and tensile strength [30, 31].

Specifically, alpha/beta titanium alloys such as Ti64, can have several alpha crystallographic orientations (variants) within each β grain. The orientations are dictated by the classical burger relationship in which $\{110\}_\beta$ II $(0001)_\alpha$ and $\langle 1\bar{1}\bar{1}\rangle_\beta$ II $\langle 2\bar{1}\bar{1}0\rangle_\alpha$. Therefore, because there is a total of six $\{110\}$ planes each with two $\langle 111\rangle$ directions, the total number of alpha variations that can occur within a β grain is 12 [29, 32]. If all 12 variants occurred, the texture is considered to be weak, however, in most cases only several variants occur within each β grain [29]. In addition, one common way to measure material crystallographic texture is by utilizing electron backscatter diffraction (EBSD) with pole figures (PF) and inverse pole figure maps (IPF maps).

1.3.4 Selective Laser Melting of Ti-6Al-4V

Within the last decade, SLM has shown promise in being able to fabricate fully dense titanium alloys [33, 34]. In SLM of $\alpha+\beta$ titanium alloys such as Ti64, the microstructure consists of columnar β grains that follow the direction of the heat flow and grow parallel to the deposit's thickness. In addition, each beta grain contains a fine α platelet martensitic structure due to the rapid cooling of the process. Prior investigations in SLM Ti64 mechanical properties has shown that SLM components tensile strength greatly depends on the pull direction and porosity of the component [35, 36]. Also, the addition of heat treatments after each build fabrication has improved ductility in SLM Ti64 components [36]. Furthermore, fatigue properties of SLM Ti64 components are generally worse

when compared to conventional made Ti64 components [37]. Nevertheless, heat treatments have been utilized to increase the fatigue strength of the SLM component by reducing porosity and internal residual stress [37]. Finally, the development of large residual stress in SLM Ti64 has been documented in several instances [14, 37].

1.4 Stress Overview

1.4.1 Applied Stress

In mechanics, the total stress imposed on a component is the summation of applied and residual stress (Equation 2). Applied stress occurs when an object is subject to an external force and can be generated by applying a transverse, torsional, or axial load. Moreover, transverse loads lead to bending and defection, axial loads lead to stretching or contraction, and torsional loads lead to twisting of the material being loaded. Each of these loading scenarios results in the development of compression, tensile, or shear applied stress and can lead to elastic or plastic deformation. In most instances, if a stress free component is not plastically deformed during the loading process, the total stress will return to zero once the applied load is removed. However, if the applied load gives rise to nonuniform plastic deformation, residual stress will develop, thus affecting the unloaded stress state of the component.

One common way to describe stresses is by utilizing the stress tensor (Equation 3). In a 3D example such as a cube, applied stress can occur on each surface in the x, y, and z direction. Therefore, a total of 9 stress elements must be utilized to fully describe the stress at any given point in the cube. Furthermore,

by using simple stress transformation equations, the stress tensor denoted in Equation 3 can be converted to principal stresses in Equation 4. In Equation 4, all shear stresses in each plane are equal to zero and thus, only three stress directions remain.

$$\sigma_{Total} = \sigma_{Applied} + \sigma_{Residual} \tag{2}$$

$$\sigma_{ij} = \begin{bmatrix} \sigma_{xx} & \sigma_{xy} & \sigma_{xz} \\ \sigma_{yx} & \sigma_{yy} & \sigma_{yz} \\ \sigma_{zx} & \sigma_{zy} & \sigma_{zz} \end{bmatrix} \tag{3}$$

$$\sigma_p = \begin{bmatrix} \sigma_{11} & 0 & 0 \\ 0 & \sigma_{22} & 0 \\ 0 & 0 & \sigma_{33} \end{bmatrix} \tag{4}$$

1.4.2 Residual Stress

Similar to applied stress, residual stress can be compressive or tensile and range in magnitude from Pa to GPa. Residual stress is formally defined as the presence of stress in a material when no loading or force is applied from the surrounding environment [39]. One common way to characterize residual stress is by the length scale in which it extends [40]. Type I macro residual stress occurs over large amounts of grains or stretches across the entire component. Type II micro residual stress occurs because of anisotropic texture or different grain orientations which often transpires in polycrystalline material. Finally, Type III micro residual stress occurs on the smallest scale because of crystalline defects (e.g. interstitials and vacancies).

The development of residual stress can occur through mechanical or thermal changes and can influence a component's fatigue life, distortion, corrosive resistance, and brittle fracture [39, 40]. In this regard, three possible origins of residual stress are material phase transformation, non-uniform shrinkage during cooling, and a difference in plastic flow caused by applied stress [39]. All three of these residual stress origins may occur in material processing procedures such as material deformation, quenching, and machining [39, 41]. However, in some instances heat treatments can often be utilized to help reduce the residual stress induced in the component. Furthermore, residual stress in a component must always maintain force and moment equilibrium because no external loads are being applied.

Residual stress can often negatively affect the mechanical properties of a component. However, there are several instances where it enables better component performance. For aerospace applications in which aircraft components are serviced and utilized for long durations, residual stress must be controlled in order to reduce the probability of premature failure. One process commonly used on aerospace components to increase fatigue and fretting fatigue strength by inducing residual stress is shot peening [41]. During shot peening, high velocity balls are shot at a component inducing compressive surface residual stress. Compressive surface residual stress helps negate surface crack propagation and thus, prolongs the fatigue life of the component. Concrete is another example that can utilize residual stress to benefit material properties [42]. Without the addition of compressive residual stress, concrete has

17

a relatively low tensile strength. However, if concrete is prestressed by compressive stress, it gains the ability to withstand larger applied tensile stresses.

On the other hand, quenching a material after heat treatment leads to fast cooling rates that cause different regions of the component to contract at different rates. This non-uniform shrinkage negatively affects the integrity of the component by creating the development of unwanted residual stress and intergranular thermal cracking. Similar to the quenching operation, the AM process typically generates undesirable residual stress and distortion that may force the AM component to delaminate off the build plate and lose its dimensional accuracy. Each time a build failure occurs, time and material is wasted and hence, the cost of the component is increased. Therefore, it is essential that residual stress is monitored during and after each AM fabrication.

1.5 Residual Stress Measurement Techniques

Current residual stress measurement techniques are classified into three broad categories: non-destructive, semi-destructive, and destructive (Figure 8). In each of these techniques, residual stress cannot be directly measured because it is an extrinsic property. Therefore, intrinsic properties such as strain, deflection, and forces must be measured first in order to calculate residual stress using elastic equations. Non-destructive methods (e.g. x-ray diffraction, Raman spectroscopy, and neutron diffraction) often measure an intrinsic parameter that is related to stress without removing the component's material. The set up and preparation time needed for non-destructive measurements is usually miniscule

when compared to destructive techniques, thus decreasing the cost of the

measurements [39]. Non-destructive measurements are typically implemented to

evaluate fatigue related residual stress imposed on a structural component that is

still in service. This helps reduce the occurrence of unexpected structural failure

in an operational component.
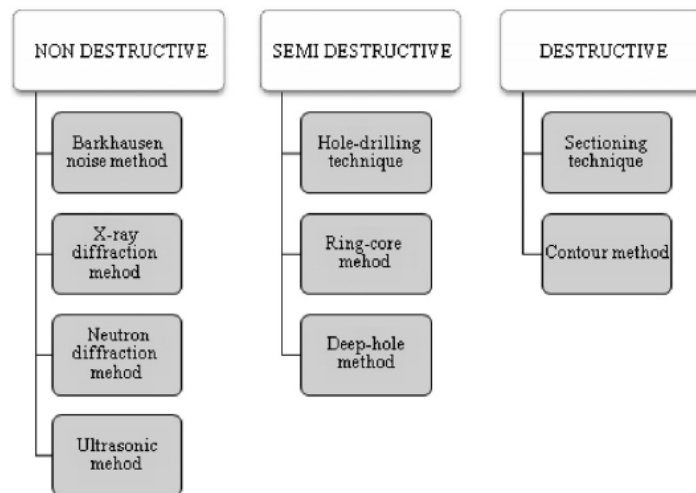
Figure 8: Three types of residual stress characterization: nondestructive, semi destructive, and destructive
[39]

Semi destructive and destructive techniques measure residual stress

through material removal and release of residual stress [39]. Notable semi-

destructive methods consist of hole drilling and ring-coring, while the contour and

layer removal methods are well known destructive techniques. Each of these

methods measures the relaxation of residual stress by drilling or sectioning.

During material removal, the residual stress must redistribute to re-establish

equilibrium, and a device is used to measure the deformation or strain. The

measured parameter enables the original stress state of the removed material to

be calculated.

1.5.1 X-Ray Diffraction

X-ray diffraction (XRD) is a non-destructive technique that utilizes x-rays similar to a strain gauge to measure the change in a material's crystal lattice. In order to measure strain, x-rays are output by the radiation source, perpendicular to the sample's surface and are diffracted at various 2θ (Bragg) angles that follow Bragg's equation (Equation 5). In (5), n is an integer, λ is the wavelength of the x-rays, d is the lattice spacing of the atoms, and θ is the angle in which the x-rays contact the surface of the crystal. The diffracted x-rays are collected by the system's detectors, and each time the Bragg equation is satisfied for a material, a *2θ* peak ensues. While XRD has good spatial resolution, the incoming X-rays have limited penetration depth [39].

$$n\lambda = 2dsin\theta \tag{5}$$

For each XRD residual stress measurement, a *2θ* angle greater than 120° is typically desired because it allows for higher precision and accuracy [14]. In the stress relieved condition, a material contains an unstressed lattice spacing of d_0 and a corresponding Bragg angle of *2θ_o*. When residual stress development occurs, the lattice spacing of the material is forced to contract or expand and thus, the lattice spacing deviates to d_1. Therefore, the resulting Bragg angle is changed to *2θ_1*. Moreover, this shift in *2θ* peaks enables lattice strain to be calculated through Equation 6. Therefore, by utilizing known material constants and assuming linear elastic distortion, the residual stress can be calculated. However, one limitation of this method is it relies on the correct d_0 value which is often hard to correctly obtain [42].

20

$$\varepsilon_L = \frac{d_1 - d_0}{d_0} \tag{6}$$

The $sin^2\Psi$ technique is commonly used and reduces the importance of d_0 for residual stress measurements [43]. During the $sin^2\Psi$ technique, multiple Ψ angle tilts are utilized and the average lattice spacing at each tilt is averaged into d_ψ. The d for each Ψ is plotted vs the corresponding $sin^2\Psi$ value and the slope of the data is utilized to calculate residual stress. The $sin^2\Psi$ technique calculates in-plane surface residual stress. In addition, the slope of the d vs $sin^2\Psi$ graph indicates if out of plane strain exists. If the measured d vs $sin^2\Psi$ slope is linear, then no out of plane strain exists. However, if the slope of the d vs $sin^2\Psi$ is parabolic, then out of plane strain exists. Additionally, XRD has been utilized to measure residual stress in metal AM components on several occasions [14, 44, 45]. In all instances, residual stress was measured only on the surface of the component.

1.5.2 Hole Drilling

Hole-drilling is a widely used semi destructive residual stress technique and is capable of measuring Type I residual stress [46]. The hole drilling technique is relatively quick and cost effective compared to other relaxation techniques and can be applied to a wide variety of materials. One advantage of the hole drilling technique is it can measure residual stress both at the surface and at various depths. Nevertheless, disadvantages of the hole drilling technique include: the material is assumed to be isotropic and the stress gradient in the hole region is assumed to be small [47]. Several notable attempts of applying the hole drilling technique to measure residual stress in AM were undertaken in [48, 49].
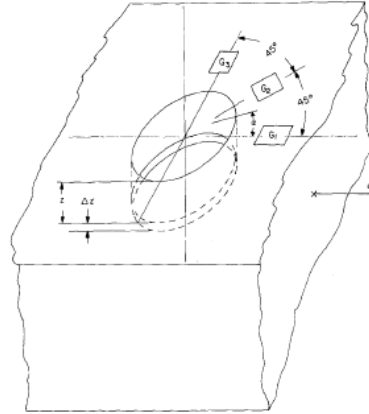
Figure 9: Schematic of strain gauge positioning in reference to a hole drilling location [50]

For hole drilling residual stress measurements, strain gauges are typically fastened on the surface several *mm* radially away from the hole drilling location at 0°, 45°, 90° or 0°, -135°, -270° (Figure 9). The technique drills a small diameter drill bit (of 1.8 mm average diameter to a depth of approximately 2 mm) into the component [51]. The drill bit is drilled into the component at speeds and a force that does not induce additional residual stress during the process. As the stressed material is removed by the drill bit, the local stresses redistribute around the drilled region and strain gauges at the surface are utilized to measure the strain change. This method enables the initial in-plane stress imposed on the surface to be calculated. A tensile surface residual stress leads to results seen in Figure 10, while a compressive surface residual stress would have the opposite effect [51].

Figure 10: The outcome of the hole drilling procedure removing tensile residual stress on the surface [51]

1.5.3 Contour Method

The contour method is a newer residual stress measurement technique that was developed in the 2000's. In this method, a component is sectioned and the residual stress perpendicular to the cut surface is relaxed. As the surface is relaxed, deformations in the plane of the cut surface enable the original residual stress state to be calculated [52]. Compressive stresses will cause the sectioned surface to expand outwards, while tensile stresses will have the opposite effect on the sectioned surface, similar to Figure 11. Therefore, the stress needed to return the sectioned surface to a non-deformed state represents the original residual stress of the component.
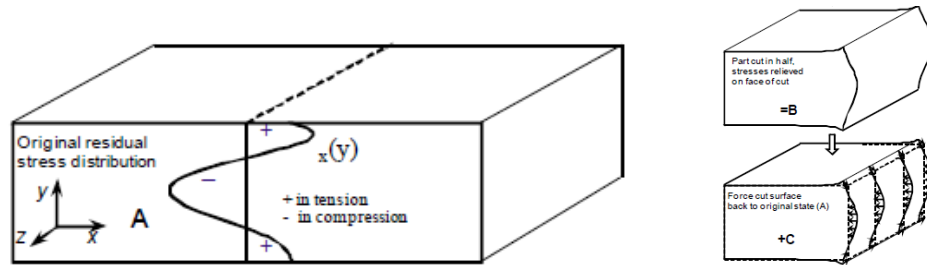
Figure 11: An EDM sectioned component showing regions with tensile and compressive residual stress and their appropriate distortion when sectioned. The contour method measures these distortions and FEA simulations are used to determine the initial stress on the cut region. [52]

As described in [52], sectioning of the component must be done carefully in order to reduce experimental error. Ideally, the most desired cut includes a small width and produces no thermal stress during the sectioning operation. Therefore, an EDM is traditionally used for the sectioning. The specimen is typical clamped during the sectioning procedure to increase contour accuracy and surface deflection is measured by a laser line profilometer or coordinate measuring machine. The surface deviations are collected and transformed into residual

stress via FEA simulations that generate 2D cross-sectional-residual-stress maps.

Generally, traditional relaxation methods such as hole drilling and sectioning, measure residual stress by strain gauges that are a set distance away from the relaxation procedure [52]. Thus, a complex equation must be used to correct for this distance. One advantage of the contour measurement is that residual stress is measured directly on the cut surface. This method can also be implemented on a wide variety of geometric components. However, spatial resolution is limited, and residual stress near the edges of the sectioned plane are assumed to be inaccurate. Work in [14, 53] are two instances in which the contour method was utilized to measure residual stress in AM.

1.5.4 Layer Removal Technique

Similar to the contour method, the layer removal method is another destructive technique that is useful in measuring residual stresses throughout the thickness of the component. In this method, strain gauges are positioned on the bottom of the sample and small thickness slices are sectioned from the top surface parallel to the strain gauges (Figure 12) [54]. As slices are removed, the component's forces and moments become unbalanced, hence the stresses redistribute to maintain equilibrium. The strain gauges measure the average redistribution of stress after each removed layer and the measurements are assumed to occur elastically. Typically the cutting mechanism used to section each slice should produce low thermal stress. An EDM and chemical etching are generally used for this sectioning method. After each slice the strain gauges are

connected to a readout box and the change in voltage is measured. The voltage is converted to strain and by utilizing a series of simple equations, the stress can be calculated. Thus far, the layer removal method has not been utilized to measure residual stress in AM.
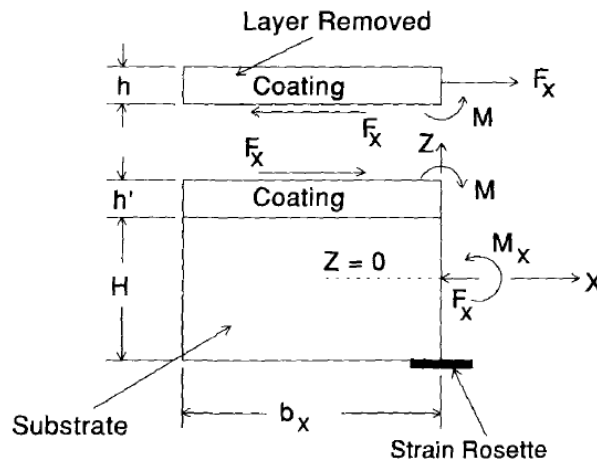
Figure 12: Mechanics behind the layer removal method [54]

1.6 Development of Residual Stress and Distortion in AM

The development of residual stress and distortion in AM is primarily influenced by several unavoidable thermal and mechanical mechanisms. Each time material is added, large thermal energy must be used to fuse the added layer to the solidified material below. The large temperature difference between the top and bottom of the AM deposit and low heat transmission between each layer enables a large thermal gradient to occur [49]. Also, as the added material cools quickly, it solidifies and contracts non-uniformly. Furthermore, during cooling, the added material is confined by the underlying material. Thus, large thermal gradients, rapid cooling rates, and confinement of the underlying material give rise to the development of residual stress and distortion in AM. However, despite the negative impact of residual stress on AM components, limited work

exists on establishing a methodology to control and reduce it during the process. As described next, some notable attempts to control the development of residual stress in AM include: tailoring energy density variables (e.g. laser power, scan speed, layer thickness, and hatch spacing), preheating temperatures, and scan strategies.

1.6.1 The Effect of Energy Density on Residual Stress

Controlling melt pool size is one method that has been investigated to reduce cooling rates and thermal gradients throughout the AM process. In this approach, process parameters associated with the energy density equation are often tailored to alter the shape and size of the processes melt pool. Through this alteration, the cooling rates and thermal gradients of the melt pool can be lowered. However, because fully dense AM components are generally needed, the tailoring of only one process parameter is not a sufficient method to change melt pool geometry.

Perhaps two of the most widely examined process parameters in the energy density equation are laser power and scan speed. In this regard, work undertaken by [19], evaluated the effect of cooling rates and thermal gradients on residual stress in the AM process. The author in [19] suggested that slower scan speeds, higher laser powers, and higher preheat temperatures lowered thermal gradients and reduced the magnitude of residual stress. Gockel et al. in 2013 established a process mapping model that predicted cooling rates and microstructure of various melt pool sizes for AM Ti-6Al-4V [55]. Gockel's work

revealed that melt pool size was increased by an increase in laser power and a decrease in scan speed.

One notable experimental investigation that further validated these modelling attempts was done by Vrancken et al [14] in 2016. In Vrancken's work, a design of experiments (DoE) was developed to evaluate the effect of laser power, scan speed, and layer thickness combinations on top surface residual stress in SLM. The author used XRD to measure the top surface residual stress on each deposit and also implemented contour measurements on several builds. The author's conclusions were that higher laser power, slower scan speeds, and larger layer thickness all reduced top surface residual stress. In addition, a regression equation of residual stress and distortion was developed from the authors work.

1.6.2 The Effect of Preheating on Residual Stress

Applying a preheat temperature to the substrate and build material is another notable technique that has been studied in an attempt to reduce the development of residual stress in AM [19, 44, 56, 14]. EBM processes such as ARCAM, utilize this methodology by pre-sintering the entire powder bed surface before each added layer is fused to underlying layers. This process enables the powder bed to maintain a preheated temperature throughout the entire build process and has been reported to minimize the magnitude of residual stress [16]. In processes such as SLM, preheating is typically not applied. Nevertheless, Mercelis et al., and Vrancken et al. assessed the effect of preheat temperature on residual stress and distortion in SLM [44, 57].

In work undertaken by Vrancken, four different preheat temperatures were evaluated [57]. At the highest preheat temperature (400°C) the residual stress was reduced by 50 percent. Similar conclusions were found by Mercelis et al., where a 200°C preheat temperature was utilized and residual stress was reduced [44]. However, it was noted by Vrancken that preheating at higher temperatures could lead to differences in the microstructure evolution of the deposit and could affect mechanical properties. Yet, it is agreed upon by several authors that preheating decreases thermal gradients and therefore reduces residual stress and distortion in AM processes.

1.6.3 The Effect of Scan Strategy

One additional approach investigated to reduce residual stress is utilizing different scan strategies for each added layer. A scan strategy is the pattern in which the laser beam rasters over the material being melted. Perhaps the most common scan strategies are island scanning, stripe scanning, and spiral scanning (Figure 13). Prior work has suggested that scan strategies can influence residual stress and distortion throughout the AM process [57, 58, 59, 60]. In reference to residual stress, [14, 38, 58] have proposed that residual stress parallel to the track direction of the energy source is much greater than residual stress measured perpendicular to the track direction. In addition, it has also been suggested that a decrease in scan vector length can help reduce residual stress development [14].
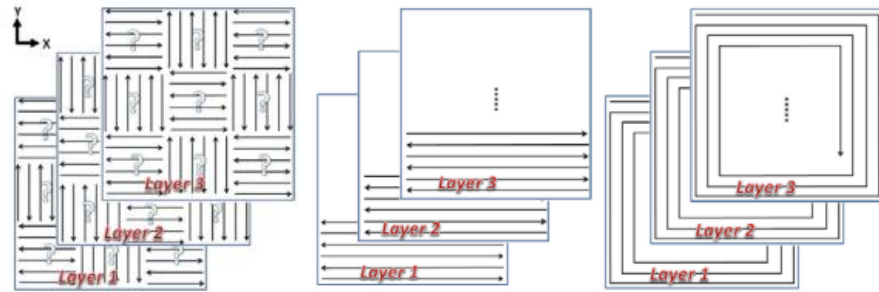
Figure 13: Common AM scan strategies: checkerboard (a), stripes (b), and spiral (c) [59]

1.6.4 Other Investigated Process Parameters

One process parameter that is not often studied to control residual stress is inter-layer dwell time. In work undertaken by Denlinger et al, several different dwell times (0, 20, and 40 seconds) were utilized to evaluate their effect on distortion and residual stress [48]. In the author's work it was suggested that shorter dwell times reduce cooling time and thermal gradients between each added layer. Hole drilling measurements enabled the author to conclude that decreasing dwell time decreased residual stress and distortion in a titanium alloy.

Finally, AM build height and AM deposit position are two process parameters that were assessed by work done by Casavola et al [49]. In their work, residual stress was measured via hole drilling at several different build heights and deposit locations. It was concluded through these measurements that residual stress decreased as a function of build height. Additionally, the deposit that was positioned in the center of the substrate developed the lowest residual stress.

1.6.5 Issues with Previous Residual Stress Work

Previous work has revealed that process parameters control and reduce the magnitude of residual stress during AM processes. Unfortunately, much of this work has focused on utilizing simulations to model the build-up of residual stress

and distortion during the AM process, while experimental work was limited. Moreover, out of the limited experimental residual stress work in AM, typically only one residual stress technique is utilized. Because each technique has its own advantages and disadvantages, it is beneficial to apply different methods to assess the validity of each.

Specifically, further experimental residual stress work in AM is currently needed to further establish the effect of process parameters on residual stress. In this regard, the effect of substrate size, shape, confinement, and condition (e.g. stress free, as-received, or machined) on the development of residual stress must also be established. Moreover, residual stress control is particularly important in processes such as SLM that often produce components with large residual stress. Hence, the work in this thesis is an attempt to fill the void of prior experimental residual stress work in SLM of Ti64.

2. THESIS CONTRIBUTIONS

The contributions of the present work are fourfold and include:

1) Experimentally established the effect of various substrate conditions on residual stress evolution of SLM deposits

2) Experimentally established the effect of SLM process parameters on residual stress in SLM deposits utilizing an initially stress free substrate

3) Evaluated (2) by utilizing several different residual stress techniques (e.g. XRD, hole drilling, contour method, and layer removal method)

4) An initial investigation of the effect of microstructure and texture evolution on residual stress development during SLM

`

3. PROJECT METHODOLOGY

3.1 Project Material

The as-received Ti-6Al-4V powder was gas atomized and had a starting composition of 90% Ti, 6% Al, and 4% V in wt. %. The average diameter of the powder was measured by Photoshop utilizing scanning electron microscope (SEM) images. The average diameter obtained through Photoshop measurements was 22.5 microns. The shape of the particles was spherical containing very few attached satellites and for each build fabrication fresh powder was used (Figure 14).
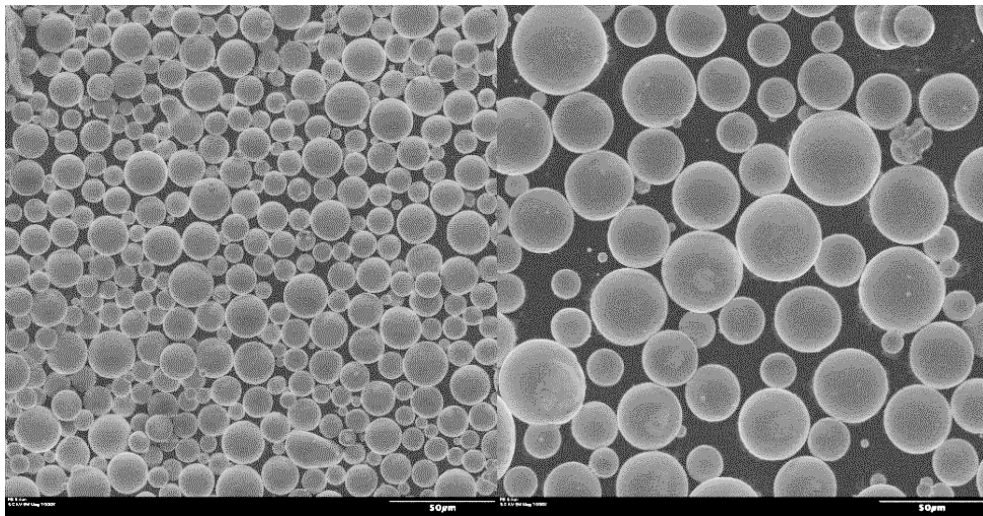
Figure 14: SEM images of the Ti64 SLM powder utilized in this work

The substrate material was cut via waterjet from a rolled Ti64 sheet. Similar to the powder, the Ti64 substrate had a starting composition of 90% Ti, 6% Al, and 4% V in wt. %. For all AM fabrications, two different size substrates were utilized (76.2 mm x 76.2 mm and 25.4 mm x 25.4 mm). Each substrate had a thickness of 7.93 mm and the starting microstructure was primarily equiaxed alpha (Figure 15). The area fraction of the alpha particles was ~ 95% and was

measured via point counting. Furthermore, the residual stress on the surface of the as-received substrate was highly compressive (513 MPa) and therefore, stress relieving procedures were utilized.
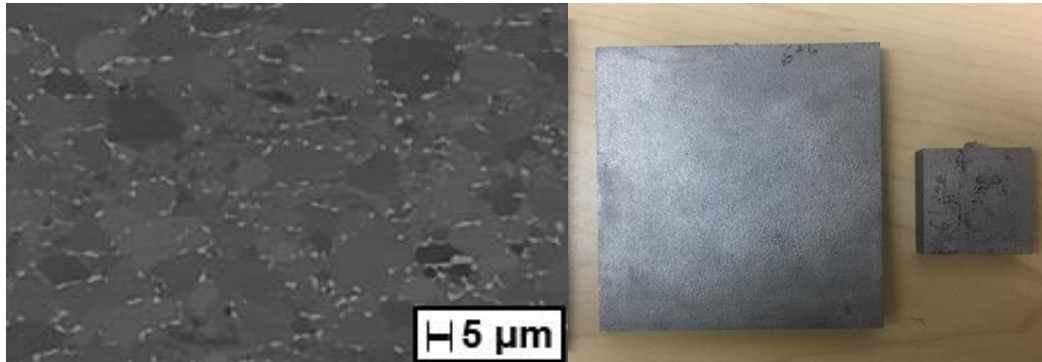
Figure 15: As-received microstructure of the substrate material (left) and the two substrates geometries utilized for experiments (right)

3.2 Substrate Heat Treatments

The goal of the heat treatment process was to produce a usable, stress-free substrate that would enable the evolution of residual stress throughout the deposit to be solely influenced by the SLM process and not by the prior stress state of the substrate. Several different heat treatments were conducted including: an alpha/beta furnace stress relief, an alpha/beta vacuum stress relief, and a beta vacuum stress relief. XRD measurements were utilized to assess the substrate's surface residual stress before and after each heat treatment. In addition, because the substrates were cut using an abrasive water jet, small excess tabs outside the substrate geometry were used to keep track of the rolling and transverse direction. After each heat treatment, these small excess tabs were cut and prepared by standard metallography for SEM imaging. The microstructure of the tab was utilized to further confirm the temperature and cooling rates of each heat treatment.

The alpha/beta furnace stress relief procedure was done in a controlled box furnace. For this procedure, each substrate was positioned in the middle of two large steel plates in an attempt to minimize distortion and oxidation on the substrate's surface. A thermocouple was positioned in the steel plate to monitor the heat treatment temperatures. Each substrate was given a heat treatment at 954°C for 1 hour and was furnace cooled. The resulting substrates were slightly oxidized, non-distorted, and stress free.

The alpha/beta vacuum stress relief and beta vacuum stress relief occurred in a controlled vacuum furnace. Before the heat treatments, each substrate was individually wrapped in tantalum foil, which reduced contamination on the surface of the substrate. An in-house jig was made to hold each substrate upright during the heat treatment. For each alpha/beta vacuum stress relief substrate, the vacuum was ramped up at 82°C/hour, held at 927°C for 1 hour, and was furnace cooled at 55°C/hour. The beta vacuum stress relief treatment was done using similar procedures, however, for this treatment the hold temperature was taken above the beta transus of the material. In addition, both vacuum stress relief treatments produced substrates that were non-oxidized, non-distorted, and stress free.

The microstructure for each heat treatment process is shown in Figure 16. Figure 17 shows the final substrate surface finish after each heat treatment. Furthermore, XRD principal residual stress measurements on each substrate condition is shown in Figure 18.
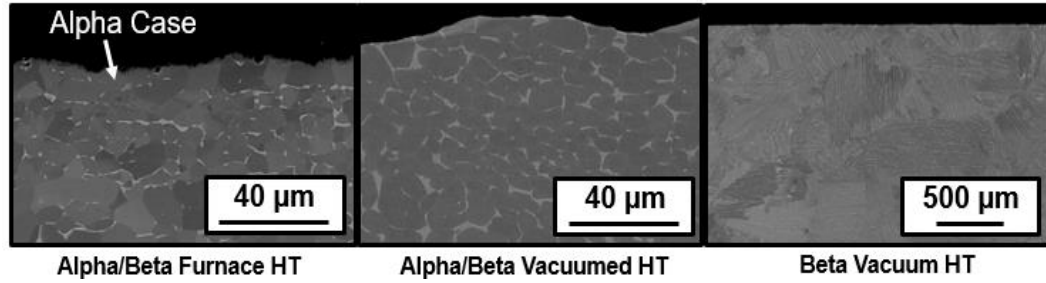
Figure 16: Substrate microstructure after each heat treatment iteration

Figure 17: Substrate surface finish after each heat treatment procedure
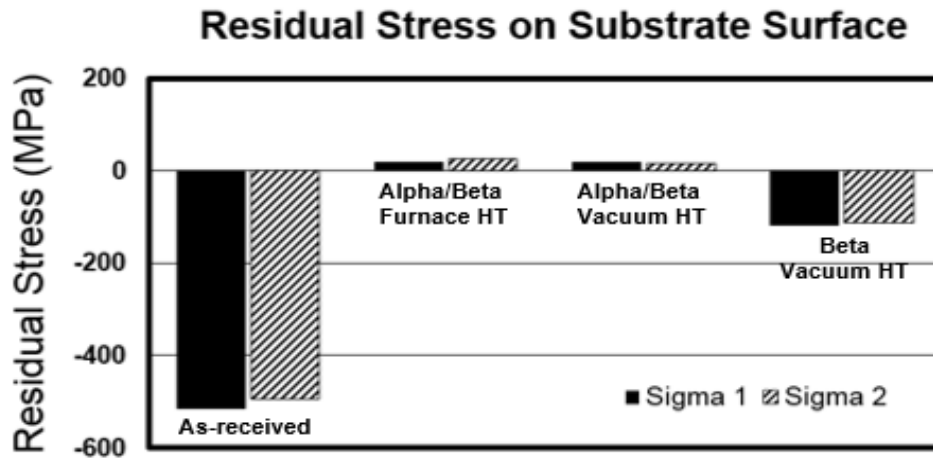
Figure 18: XRD measured residual stress on the surface of each substrate

3.3 SLM System

A SLM testbed developed by Universal Technologies Cooperation (UTC) located in Kettering, Ohio, was utilized for the fabrication of each deposit (Figure 19). The system used has the unique capability to fabricate a wide variety of materials with fully customized process parameters. The fabrication process for

each build occurred in an argon filled chamber that had several working stations. An IPG 500 W laser beam with a 50 µm spot size and focal length of 152 mm was focused onto the test bed by a series of lenses and mirrors.

Figure 19: UTC's in house built SLM system

The SLM test bed contained two actuators that controlled the movement of the build platter region and powder bay. Specifically, the build platter and powder bay both had dimensions of 102 mm x 102 mm and were designed for small substrate builds. A third actuator was used to control the movement of the raking mechanism utilized to spread powder. A custom made software was used to control each of the SLM test bed's movements and the process parameters for build fabrication. In addition, several in-process monitoring sensors evaluated the quality of each spread and melted layer. These sensors included: high speed cameras, infrared sensors, and a laser line profilometer.

Nominal process parameters for Ti64 were obtained through several initial designs of experiments (DoE). In each DoE, the laser power, scan speed, layer thickness, and hatch spacing were varied. Based on these trials the optimal/nominal process parameters were selected (Table 1).

Ti64 Nominal Parameters	
Laser Power:	300 W
Scan Speed:	400 mm/s
Hatch Spacing:	120 μm
Stripe Width:	3 mm
Layer Thickness:	50 μm
Dwell Time:	20 seconds

Table 1: Nominal process parameters utilized for Ti64 builds

3.4 Design of Experiments

As previously mentioned, the goal of the experiments designed in this work was to assess the effect of process parameters on residual stress in SLM utilizing several different residual stress measurement techniques. The process parameters evaluated were substrate condition, stripe width, laser power, build height, scan speed, build plan area, and substrate overhang. Simple build geometries such as cubes and rectangular prisms were chosen to enable a simple foundation for future simulation attempts. All substrates during the build process were unconstrained and thus, free to deform throughout the fabrication process.

In sections 3.4.1 and 3.4.2 all four prepared substrate conditions were utilized for the experiments. In sections 3.4.2 - 3.4.5 AM deposits were built in the center of their respective substrates. Trials described in sections 3.4.3 – 3.4.5 only utilized alpha/beta vacuum stress relieved substrates. The coordinate system used for each AM build and substrate is shown in Figure 20. Finally, the track direction of the laser beam for the first layer of each deposit discussed in sections 3.4.2 – 3.4.5 started in the rolling direction and for each added layer the stripe scan was rotated 67 degrees clockwise.
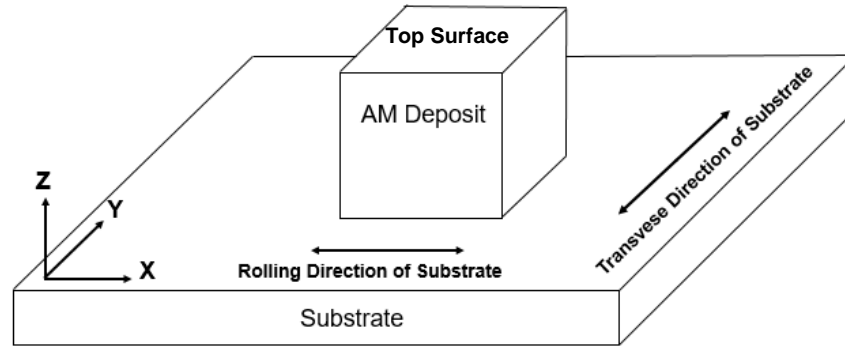
Figure 20: Substrate and AM build reference system

3.4.1 Laser Glaze Experiments

Laser glazes were utilized in this work to assess the effect of stripe width, laser power, and substrate condition on residual stress. For each laser glaze fabrication, the laser beam is turned on and rastered over the substrate material in one direction without adding any material. Therefore, the build height of each laser glaze was 0 mm. For each laser glaze fabrication, the track direction of the stripe scan strategy was parallel to the rolling direction of the substrate. All four substrate conditions (i.e. as-received, alpha/beta furnace stress relieved, alpha/beta vacuum stress relieved, and beta stress relieved) were used for the laser glaze experiments.

On each substrate condition, four 19.05 mm x 19.05 mm square laser glazed regions were fabricated onto 76.2 mm x 76.2 mm x 7.93 mm substrates (Figure 21). Each laser glazed region was positioned 19.05 mm away from neighboring glazes and from the edges of the substrate. After each laser glaze was complete, the fabrication was paused for 5 minutes and then the laser beam proceeded to the next laser glaze. This allowed temperatures of the substrate to cool down before the next glaze was scanned. In reference to Figure 21, the top left laser

glaze was fabricated with the nominal parameters shown in Table 1. The additional three laser glazed regions contained 1 to 2 set variations in process parameters. The laser glazes were fabricated in sequential order denoted by the red numbers in Figure 21. Furthermore, only XRD measurements were performed on the laser glaze builds. Specifically, XRD was performed on the top surface of each laser glaze and then the substrate was rotated 180° and XRD measurements were completed on the bottom of the substrate in the exact *x* and *y* location. The XRD scan locations are shown in in Figure 22.
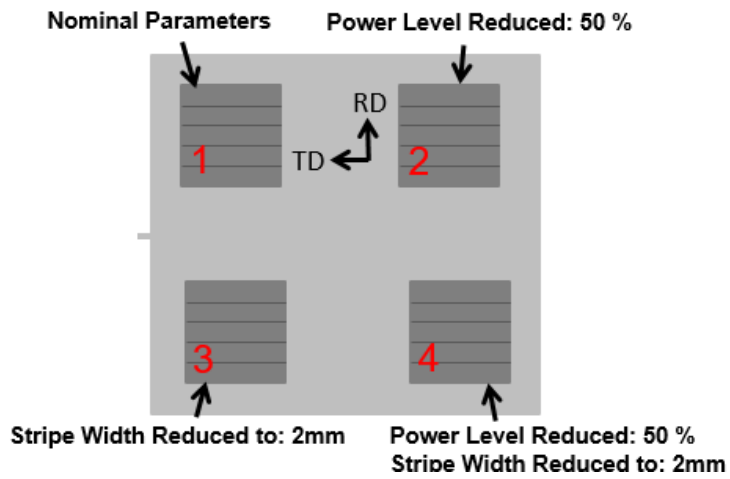
Figure 21: Overview of laser glaze fabrication with process parameters utilized
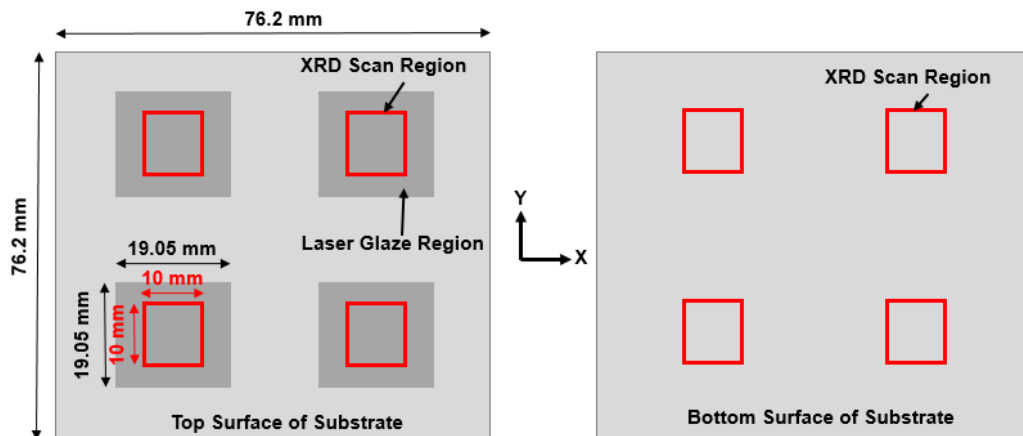
Figure 22: XRD scan strategy used for residual stress measurements completed on the laser glaze builds

3.4.2 Deposits Fabricated on Different Substrate Conditions Experiments

The effect of substrate condition on residual stress was further explored by the fabrication of 25.4 x 25.4 x 1.6 deposits onto all substrate conditions (Figure 23). All AM deposits were fabricated with nominal parameters. Similar to the laser glaze fabrications, only XRD was utilized to measure residual stress on the top surface of the AM deposit and bottom surface of the substrate. The XRD box strategy implemented on the top surface of the AM deposit and on the bottom of the substrate surface is shown in Figure 24.

Figure 23: As-received substrate with 25.4 mm x 25.4 mm x 1.6 mm SLM deposit
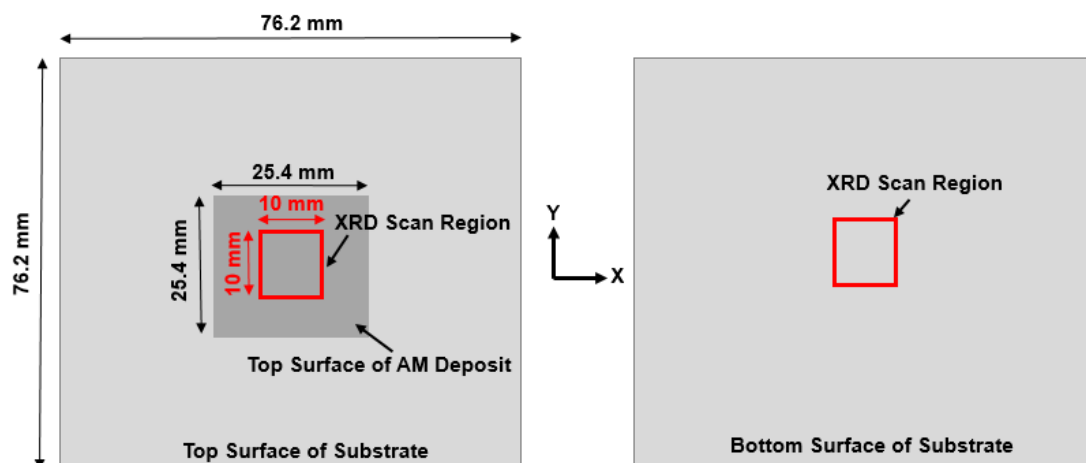
Figure 24: XRD scan strategy used for the 1.6 mm deposits

3.4.3 Effect of Build Plan Area on Residual Stress

In order to assess the effect of build plan area on residual stress, three builds were fabricated on 76.2 mm x 76.2 mm x 7.93 mm substrates. The dimensions of the three deposits were 25.4 mm x 25.4 mm, 50.8 mm x 50.8 mm, and 76.2 mm x 76.2 mm all with a build thickness of 1.6 mm (Figure 25). Therefore, the 25.4 mm x 25.4 mm x 1.6 mm deposit had a substrate overhang of 50.4 mm on all sides, the 50.8 mm x 50.8 mm x 1.6 mm deposit had a 25.4 mm overhang on all sides, and the 76.2 mm x 76.2 mm x 1.6 mm deposit had no substrate overhang. In addition, each deposit was fabricated using nominal parameters.

Similar to the first two experiments, XRD was utilized to measure the residual stress. The same XRD scan strategy shown in Figure 24 was used for the 25.4 mm x 25.4 mm x 1.6 mm AM deposit. However, the XRD box scan on the top surface of the AM deposit and the bottom surface of the substrate increased to 20 mm x 20 mm for the 50.8 mm x 50.8 mm x 1.6 mm deposit and 30 mm x 30 mm for the 76.2 mm x 76.2 mm x 1.6 mm deposit.
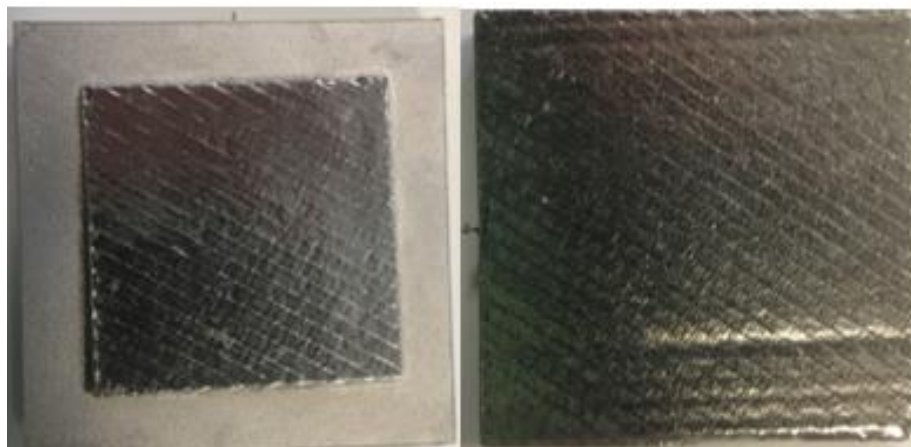
Figure 25: 50.8 mm x 50.8 mm x 1.6 mm and 76.2 mm x 76.2 mm x 1.6 mm deposits

41

3.4.4 Effect of Substrate Overhang vs. No Overhang Experiment

A series of deposits were fabricated in this work to evaluate the effect of substrate overhang and build height on residual stress. In this regard, the deposits utilized were 25.4 mm x 25.4 mm with a build height of 1.6 mm, 12.7 mm, and 25.4 mm. These three deposit heights were fabricated on both 76.2 mm x 76.2 mm x 7.93 mm and 25.4 mm x 25.4 mm x 7.93 mm substrates. Therefore, each AM deposit had a substrate overhang of 50.8 mm on the larger substrate, while AM builds fabricated on the smaller substrates had no overhang. For the substrates with no overhang a square brace was made for the fabrications that allowed the substrate to freely distort, but kept it from moving horizontally (Figure 26). In addition, one extra 25.4 mm x 25.4 mm x 25.4 mm and 25.4 mm x 25.4 mm x 14.7 mm deposit was fabricated on a 25.4 mm x 25.4 mm x 7.93 mm substrate.

Four residual stress measurement techniques were applied on the builds in this section. First, XRD scans were utilized on the top surface of the AM deposit and bottom surface of the substrate using the same XRD scheme shown in Figure 24. Next, hole drilling measurements were performed on the top surface of the deposit and bottom surface of the substrate of the three deposits that were fabricated on the 76.2 mm x 76.2 mm x 7.93 mm substrates. The contour method was employed on the largest AM deposit fabricated on the 76.2 mm x 76.2 mm x 7.93 mm substrate (after hole drilling measurements) and on the largest deposit fabricated on the 25.4 mm x 25.4 mm x 7.93 mm substrate. Last, the layer removal method was applied to a 25.4 mm x 25.4 mm x 14.7 mm and 25.4 mm x

25.4 mm x 25.4 mm deposit that were fabricated onto the 25.4 mm x 25.4 mm x 7.93 mm substrate.
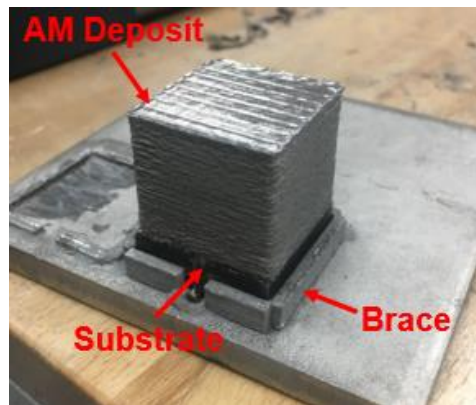
Figure 26: AM deposit with no substrate overhang

3.4.5 Effect of Scan Speed on Residual Stress

The final experiment in this work assessed the effect of scan speed on residual stress. In this regard, three 25.4 mm x 25.4 mm x 12.7 mm deposits were fabricated on 76.2 mm x 76.2 mm x 7.93 mm substrates (Figure 27). The three scan speeds used for fabrications were 400 mm/s, 700 mm/s, and 1000 mm/s. XRD was utilized on the top surface of each AM deposit and bottom surface of the substrate using the same XRD scheme shown in Figure 24. In addition, hole drilling measurements were applied on the top surfaces of the AM deposits and bottom surfaces of the substrates.
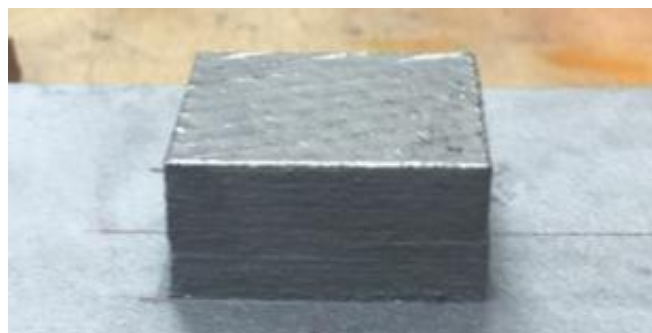
Figure 27: 25.4 mm x 25.4 mm x 12.7 mm deposit fabricated with 700 mm/s scan speed

3.5 Residual Stress Measurement Techniques

After all AM builds were fabricated, several residual stress techniques were applied to quantify the magnitude of residual stress. XRD was utilized on the top surface of each AM fabrication and the bottom surface of each substrate. The hole drilling technique was utilized selectively on several AM builds to corroborate XRD measurements. Finally, the contour and layer removal method were used to evaluate residual stress throughout the thickness of selected builds. The settings and procedures for each measuring technique are discussed in the following sections.

3.5.1 X-Ray Diffraction Measurements

XRD measurements were done on a Proto Laboratory Residual Stress Measurement System utilizing XRDWin 2.0 software. The XRDWIN 2.0 software used the d vs $sin^2\Psi$ technique and applied extensive curve fitting to measure surface residual stress. For the measurements, a Cu_K_α radiation source was output at 25 KV with a current of 20 mA. Additional XRD settings comprised of a 2θ angle of 141.5°, a 2 mm circular aperture, a box scan strategy, and a diffraction plane of (21.3). The β angles of the x-ray source ranged from -15° to 15° per measurement with 2.5° increments. Nickel detectors were used to capture the diffracted x-rays and at each β oscillation of the x-ray source 10 exposures for 5 seconds each were captured.

The d vs $sin^2\Psi$ method allows for simplification and increase in measurement speeds. By assuming zero stain exists in the out of plane direction of the XRD measurements, Equation 7 is obtained:

$$\varepsilon_{\psi\phi} = \left[\frac{1+v}{E}(\sigma_\phi)sin^2\psi\right] - \left[\frac{v}{E}(\sigma_{11}+\sigma_{22})\right] \qquad (7)$$

where

$$\sigma_\Phi = \sigma_{11}cos^2\Phi + \sigma_{22}sin^2\Phi \qquad (8)$$

and

$$\sigma_\Phi = \sigma_{11}cos^2\Phi + \sigma_{22}sin^2\Phi + \sigma_{12}sin2\Phi. \qquad (9)$$
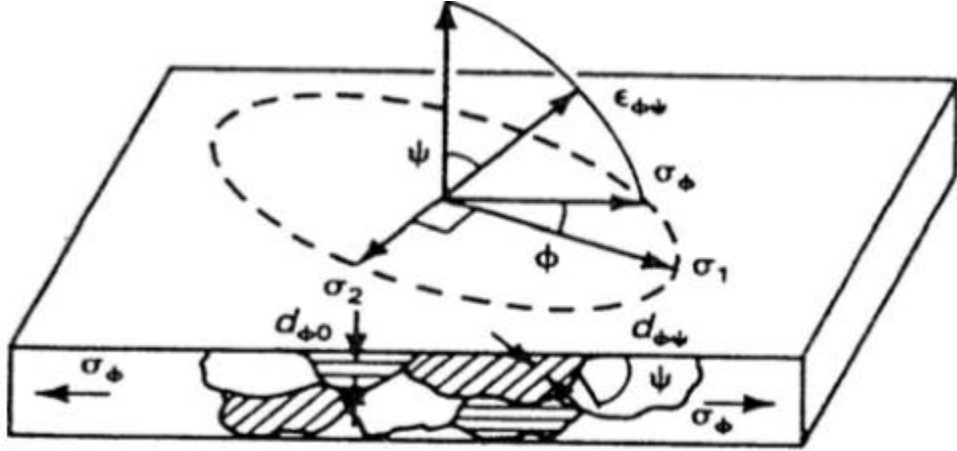
Figure 28: Measurement of stress on a plane [43]

In Equation (7), $(1+v)/E$ and v/E are elastic constants for a specific miller index plane of the material, $\varepsilon_{\psi\phi}$ is the measured strain at angles Ψ and Φ, σ_{11} and σ_{22} are principal stresses, and σ_ϕ is the stress at an angle Φ (Figure 28). In addition, Equation 8 is used when no in-plane shear stress exists and equation 9 is used when in plane shear stress exists.

Furthermore, by using the slope of the *d* vs *sin²Ψ* measurements (*m*), the residual stress in the desired direction is obtained by equation 10:

$$\sigma_\phi = \left(\frac{E}{1+v}\right)_{hkl}\left(\frac{1}{d_0}\right)(m). \qquad (10)$$

In Equation (10), $E/(1 + v)$ is the x-ray elastic constant (XEC) for a specific miller index plane. The XEC used for the measurements in this work was 84.1 GPa and was provided by [43]. A total of 60-120 XRD measurements were taken on the top surface of each AM deposit in the as-fabricated condition and on the bottom surface of each substrate. Before each measurement, the system was calibrated with a known standard for Ti64.

3.5.2 Hole Drilling Measurements

After XRD measurements, five samples were sent for hole drilling at Hill Engineering, located in Rancho Cordova, California (Figure 29). As previously mentioned, the hole drilling technique was done on the 25.4 mm x 25.4 mm x 25.4 mm, 25.4 mm x 25.4 mm x 12.7 mm, and 25.4 mm x 25.4 mm x 1.6 mm deposits fabricated with nominal parameters on the 76.2 mm x 76.2 mm x 7.93 mm substrates. In addition, hole drilling was also done on the 25.4 mm x 25.4 mm x 12.7 mm deposits fabricated with 700 mm/s and 1000 mm/s scan speeds. Before being shipped to Hill Engineering, the top surface of each deposit was machined to reduce top surface roughness on the AM component. Thus, the machining operation slightly changed the total thickness of the deposit (Table 2).

AM Deposit (Length x Width x Height) (mm)	Process Parameters	Height After EDM (mm)
25.4 x 25.4 x 25.4	Nominal	25.24
25.4 x 25.4 x 12.7	Nominal	12.45
25.4 x 25.4 x 12.7	Nominal -w- 700 mm/s	12.54
25.4 x 25.4 x 12.7	Nominal -w- 1000mm/s	12.57
25.4 x 25.4 x 1.6	Nominal	1.48

Table 2: Sample height after the top surface was machined for hole drilling measurements
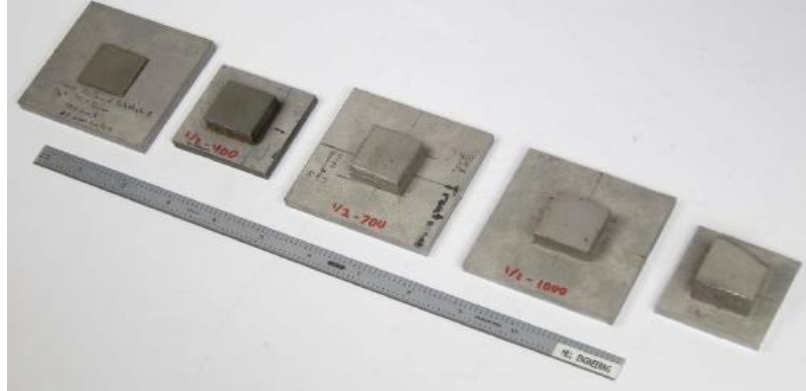
Figure 29: The five AM deposits that received hole drilling measurements

The hole drilling measurements were performed on the top surface of each AM deposit and on the bottom surface of each substrate. The measurements were done in the center of their respective surfaces. Also, on the tallest build (25.4 mm x 25.4 mm x 25.4 mm), hole drilling measurements were done on the side surface of the deposit at two different heights (Figure 30). The drill bit used for hole drilling measurements had a 2 mm diameter and all measurements went to a depth of 1 mm. Strain gauges were positioned around the hole drilling location at 0°, 45°, and 90°. For the measurements, standard Ti64 material properties were used and included: a Poisson's ratio of 0.33 and a bulk elastic modulus of 114 GPa.
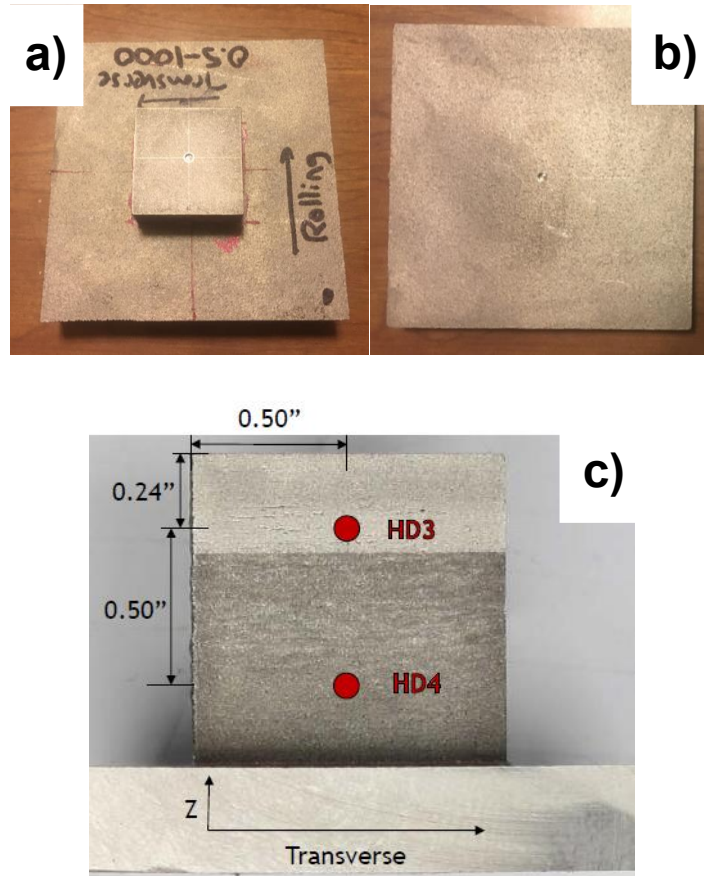
Figure 30: Hole drilling locations on the AM deposits: a) represents the top surface hole drilling location b) represents the substrate bottom surface hole drilling location, and c) represents the side surface hole drilling locations

3.5.3 Contour Method Measurements

Similar to the hole drilling measurements, the contour measurements were also performed by Hill Engineering. In order to assess the residual stress throughout the thickness of the SLM deposits, two contour measurements were performed. Contour measurements were made on the 25.4 mm x 25.4 mm x 25.4 mm deposits fabricated on the two substrate sizes. For each contour measurement, an EDM cut through the substrate in the transverse direction and proceeded up the thickness of the substrate and AM deposit. The sectioning was done in the middle of the AM deposits (Figure 31). The distortion of the cut plane

was measured and the initial residual stress on cut surface was obtained via FEA simulations.
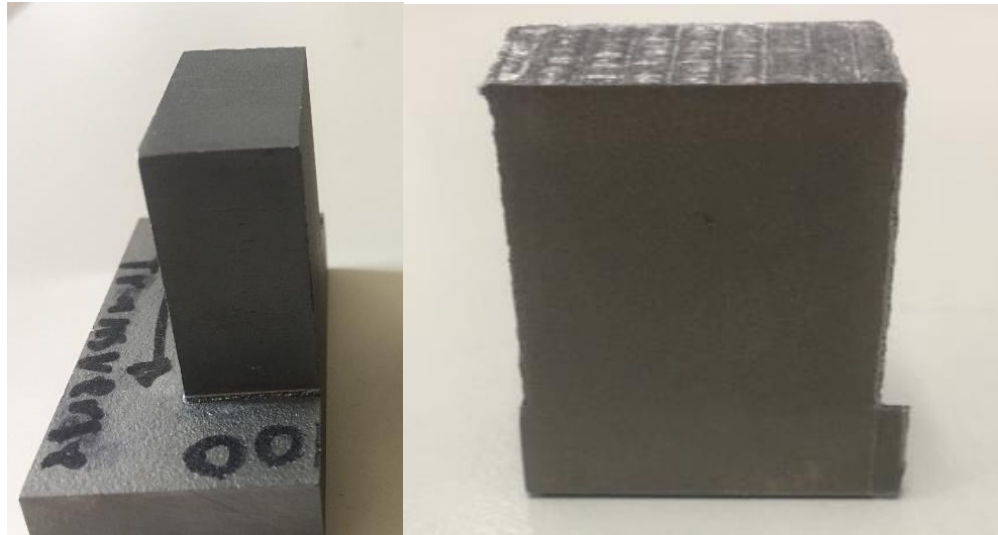
Figure 31: Sectioned plane cut by EDM for contour measurements: The EDM cut on the 25.4 mm x 25.4 mm x 25.4 mm deposit with substrate overhang is shown on the left and EDM the cut on the 25.4 mm x 25.4 mm x 25.4 mm deposit with no substrate overhang is shown on the right

3.5.4 Layer removal measurements

The layer removal method was the final utilized residual stress technique and like the contour method, measured residual stress throughout the thickness of the component. This method was applied to a 25.4 mm x 25.4 mm x 14.7 mm and 25.4 mm x 25.4 mm x 25.4 mm deposits fabricated on the 25.4 mm x 25.4 mm x 7.93 mm substrates. Four strain gauges were positioned at 0°, 45°, 90°, and 180° on the bottom surface of the substrate. The deposit material was removed by a low stress abrasive saw and slices were removed incrementally from the top surface of the deposit (Figure 32). Both AM deposits were sliced until only substrate material remained. Standard Ti64 material properties were used and included: a Poisson's ratio of 0.33 and a bulk elastic modulus of 114

GPa. The residual stress measured by the layer removal method is obtained by Equations 11 and 12:

$$\sigma_x = \frac{E}{1-v^2}\left[2\varepsilon_x + \frac{W}{2}\frac{d\varepsilon_x}{dW}\right.$$

$$-3W\int_W^{W_i}\frac{\varepsilon_x}{W^2}dW + 2v\varepsilon_y + v\frac{W}{2}\frac{d\varepsilon_y}{dW} \quad (11)$$

$$\left.-3vW\int_W^{W_i}\frac{\varepsilon_y}{W^2}dW\right]$$

and

$$\sigma_y = \frac{E}{1-v^2}\left[2\varepsilon_y + \frac{W}{2}\frac{d\varepsilon_y}{dW}\right.$$

$$-3W\int_W^{W_i}\frac{\varepsilon_y}{W^2}dW + 2v\varepsilon_x + v\frac{W}{2}\frac{d\varepsilon_x}{dW} \quad (12)$$

$$\left.-3vW\int_W^{W_i}\frac{\varepsilon_x}{W^2}dW\right] .$$

Figure 32: AM sample prepared for layer removal method (left) and cut AM slices during the procedure (right)

In (11) and (12), ε_x is the strain measured in rolling direction, ε_y is the strain measured in the transverse direction, W_i is the initial height, W is the instantaneous height after each cut, E is the elastic modulus, and v is the Poisson's ratio. An additional Ti64 cube was stress relieved to assess if residual stress was induced during the cutting operation. The starting thickness of the specimen was 25.4 mm and the same strain gauge configuration was utilized. The specimen was sliced until the thickness reached 4 mm.

3.6 Microstructure and Texture Analysis

Because the residual stress was expected to vary throughout the depth of the AM build, microstructure and texture analysis were completed throughout the thickness of the substrate and AM material. Standard metallography was performed on the cut surface made by the contour measurement on the 25.4 mm x 25.4 mm x 25.4 mm deposit with the 76.2 mm x 76.2 x 7.93 substrate. Backscatter electron (BSE) images were taken in the green regions shown in Figure 33. The microscope settings for the images were a voltage of 15KV, a spot size of 4, and the magnifications utilized were 500x, 1000x, and 2000x. Images were taken of the bottom substrate region, the first melted region of the substrate, the mid height of the AM deposit, and the top surface of the AM deposit. The BSE images enabled the effect of residual stress on microstructure evolution to be investigated.
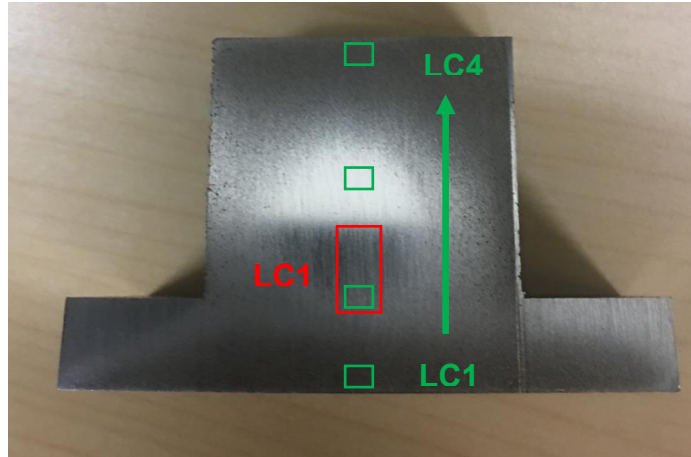
Figure 33: Montage locations for BSE images and EBSD: BSE image locations are shown by the 4 green denoted squares and the EBSD location is denoted by the red rectangle region

For crystallographic texture analysis, an electron backscatter diffraction scan was performed on the prepared surface. The goal of the scan was to determine if the residual stress affected the crystallographic texture of the AM build. The EBSD scan for location 1 started 1 mm below the substrate material and went several *mm* up the build thickness of the AM deposit. The alpha phase of the material was collected for the EBSD analysis. Pole figures and inverse pole figure maps were determined at the location to help further understand the preferred orientation of the crystallographic texture.

The EDAX EBSD coordinate system utilized in this work is illustrated in Figure 34. In this regard, the RD and TD are in the plane of the EBSD scan while the ND is perpendicular to the surface. For the scans, the build direction of the SLM deposit was parallel to the TD, the rolling direction of the substrate was parallel to the ND, and the transverse direction of the substrate was parallel to the RD. An IPF map was collected in the ND direction for the EBSD motage

location shown in Figure 33. In addition, PF in the $(000\bar{1})$, $(10\bar{1}1)$, and $(11\bar{2}0)$

were calculated in the montage location.
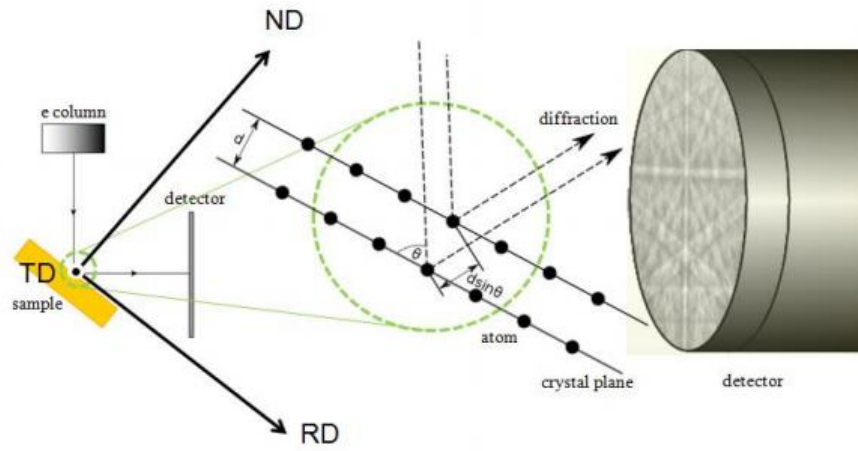
Figure 34: EDAX EBSD coordinate system utilized for this work [61]

4. XRD RESULTS AND DISCUSSION

4.1 Chapter Overview

In this chapter, XRD results are summarized and discussed. XRD was the most utilized residual stress technique and the measurements revealed several surface residual stress trends. As previously mentioned, all XRD measurements were done on the as-deposited SLM surface and bottom surface of the substrate. The residual stress measurements shown and discussed in this chapter are the principal stresses measured on each surface (corresponding to σ_{11} and σ_{22}).

4.2 Laser Glaze Results

The effect of several process parameters on residual stress were investigated by XRD measurements completed on the laser glaze regions fabricated on the four substrate conditions. The four substrate conditions that were utilized are discussed in section 3.2. As expected, the laser glaze microstructure contained high levels of martensitic alpha phase because of the rapid cooling rates of the melted material (Figure 35). The beta grains in the laser glaze melted region comprised of an equaixed geometry after cooling because no material was added.
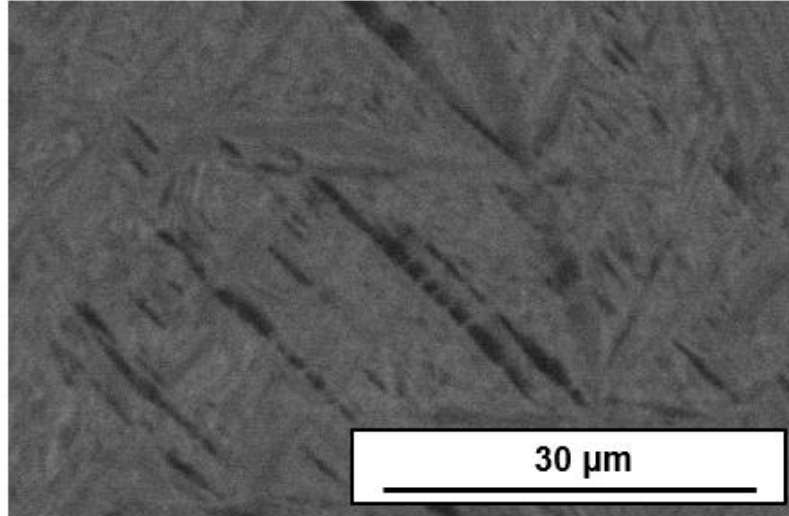
Figure 35: BSE image of microstructure of melted laser glaze region

Figure 36 shows the top surface residual stress measured on the laser glaze

regions that were fabricated with nominal parameters on the four different

substrate conditions. Moreover, the top surface residual stress measured on the

laser glazes with a 50 percent power reduction and a 33 percent stripe reduction

are shown in Figures 37 and 38 respectively. Each laser glaze region in Figures

36, 37, and 38 exhibited tensile residual stress on the top surface and exhibited a

noticeable directionality. Moreover, the largest principal direction was within ±8°

from the track direction of the laser beam, which is in agreement with prior

literature [14]. In comparing Figures 36 and 37, the residual stress noticeably

increased in the laser glazes fabricated with a 50 percent power reduction. The

likely explanation for this trend was the difference in the melt pool sizes and

cooling rates. In this regard, the laser glaze fabricated with nominal parameters

had a much larger melt pool than the laser glaze fabricated with a 50 percent

power reduction. Specifically, the measured melted depth of the nominal

parameter laser glaze was approximately 207 microns, while the 50 percent

power reduction laser glaze had an average melted depth of 143 microns. Therefore, the increase in melt pool size of the nominal parameter laser glaze enabled the melted region to have slower cooling rates and lower thermal gradients. This allowed the residual stress magnitude to be reduced.

In addition to increasing laser power, there was also a noticeable decrease in residual stress when the vector width of the stripe scan was decreased from 3 mm to 2 mm. Prior work had suggested that reducing scan vectors was beneficial in reducing the development of residual stress during the SLM process. In comparing Figures 36 and 38, this trend was apparent and was in agreement with prior work. Furthermore, XRD measurements were completed on the bottom surface of the laser glaze substrates. The bottom surface of the substrates had no change in residual stress from their initial state. Hence, the bottom surface residual stress was not affected by the laser glaze fabrication.

Perhaps the most noticeable trend shown in the laser glaze measurements was that the residual stress on the top surface was always the greatest in the as-received substrate. Unfortunately, in much of prior work the initial substrate stress condition was often unknown and not discussed in detail. Yet, in Figures 36, 37, and 38 the condition of the substrate tremendously affected the top surface residual stress in the laser glaze regions.

Nominal Parameters Laser Glaze
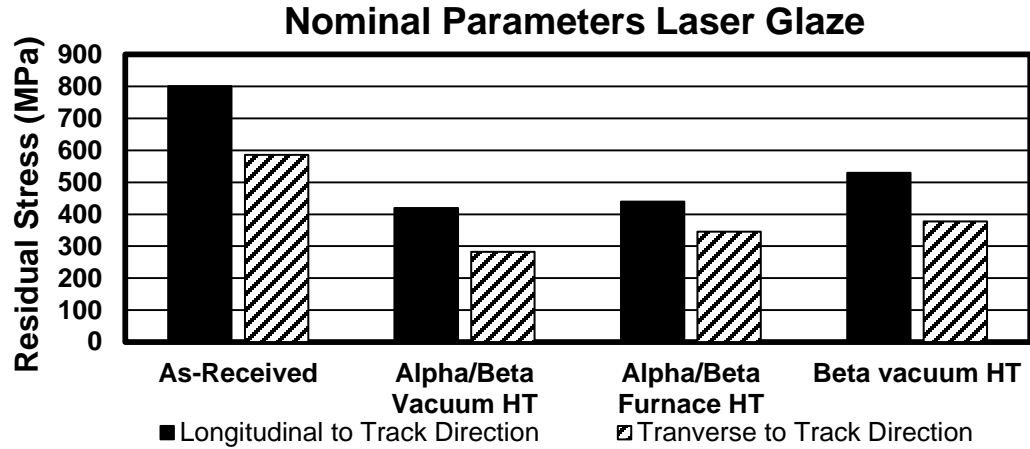
Figure 36: Top surface residual stress measured via XRD on the laser glazes fabricated with nominal parameters on the four prepared substrate conditions

50 % Power Reduction Laser Glaze
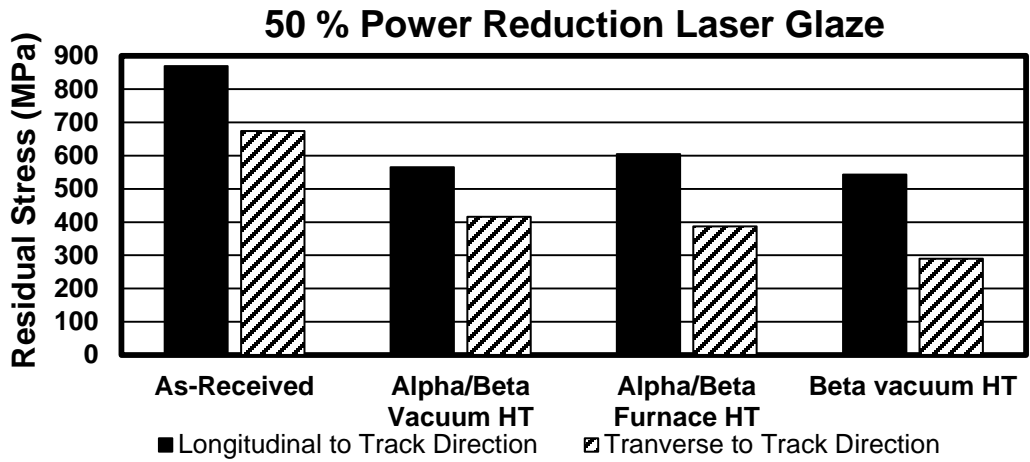
Figure 37: Top surface residual stress measured via XRD on the laser glazes fabricated with a 50% percent power reduction on the four prepared substrate conditions

33 % Stripe Reduction Laser Glaze
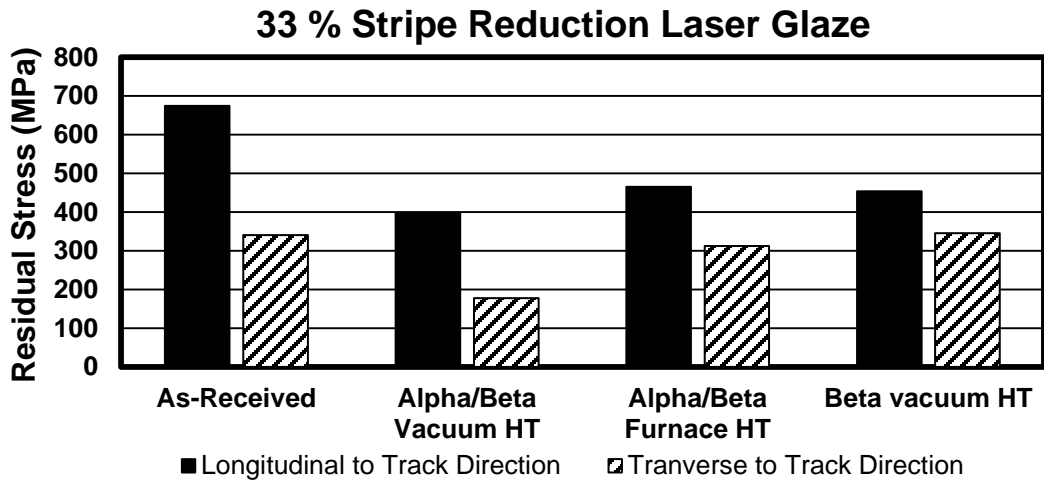
Figure 38: Top surface residual stress measured via XRD on the laser glazes fabricated with a 33% stripe reduction on the four prepared substrate conditions

A possible explanation for the difference in top surface residual stress was the difference in the substrate residual stress prior to the fabrication. The as-received substrate had highly compressive residual stress on all surfaces that were balanced by tensile residual stress throughout the thickness of the material. However, the stress relieved substrates exhibited low to no residual stress on the surface and throughout the thickness. In the as-received substrate condition, the melt pool of the laser glaze fabrication relieved the compressive layer of residual stress on the top surface of the substrate. Hence, the top surface laser glaze residual stress in the as-received substrate was the summation of the tensile stress in the thickness of the substrate and the tensile stress developed from the shrinkage of the melted region. On the contrary, the tensile surface residual stress developed in the laser glaze regions fabricated on the stress relieved substrates purely evolved from the shrinkage of the melted region. Thus, the resulting residual stress was lower in the laser glazes that were fabricated on stress relieved substrates.

4.3 Substrate Condition Results

The effect of substrate condition was further investigated by the fabrication of 25.4 x 25.4 x 1.6 mm SLM deposits onto the four prepared substrate conditions. Unfortunately, an SLM deposit could not be fabricated on the alpha/beta furnace heat treated substrate. This was because of the alpha case that was present on the substrates surface. Alpha case occurs in titanium alloys when the material is heated in an oxygen rich environment (such as a furnace) and is a brittle surface

58

layer that is prone to micro cracking. Each SLM build that was attempted on this substrate condition separated from the substrate by the 20th layer.

The measured top surface residual stress on the successful builds is shown in Figure 39. Interestingly, the prior substrate residual stress continued to affect the top surface residual stress up to a build height of 1.6 mm. In this regard, the top surface of the deposit fabricated on the as-received substrate had residual stress that was 100 – 200 MPa greater than the SLM deposits fabricated on the two stress relieved substrate conditions. On each SLM deposit the largest principal stress was parallel to the track direction of the final scanned layer. Also, the as-received bottom substrate surface residual stress was decreased from its prior state but remained in compression after the 1.6 mm fabrication (Figure 40). However, the bottom surfaces of the two stress relieved substrates were in tension after the 1.6 mm fabrications.
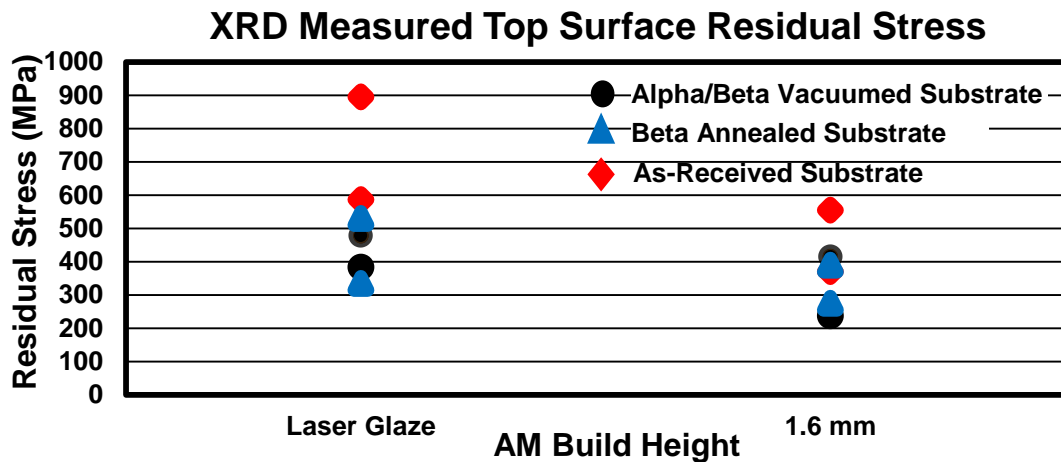
Figure 39: Top surface residual stress measured via XRD on the nominal parameter laser glazes and successful 1.6 mm SLM deposits on the different substrate conditions
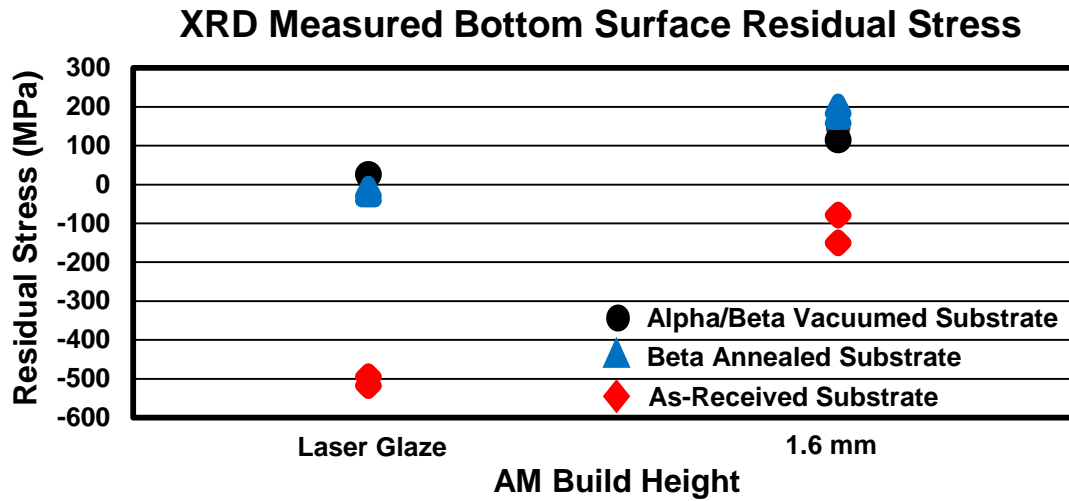
Figure 40: Bottom surface residual stress measured via XRD on the nominal parameter laser glazes and successful 1.6 mm SLM deposits on the different substrate conditions

4.4 Build Plan Area Results

The goal of the three different build plan areas was to identify the importance of AM build size and substrate size on residual stress. The measured residual stress on the top surface of the deposit and the bottom surface of the substrate are shown in Figures 41 and 42. The top surface residual stress increased slightly as the build plan area increased. Similar to the top surface observation, residual stress on the bottom surface of the substrate also increased as build plan area increased. Particularly, compared to the smallest build plan area, the largest build plan area had a 3 to 4 fold increase in residual stress on the bottom surface of the substrate. Additionally, the largest build plan area caused the largest out of plane substrate distortion.

Top Surface Residual Stress
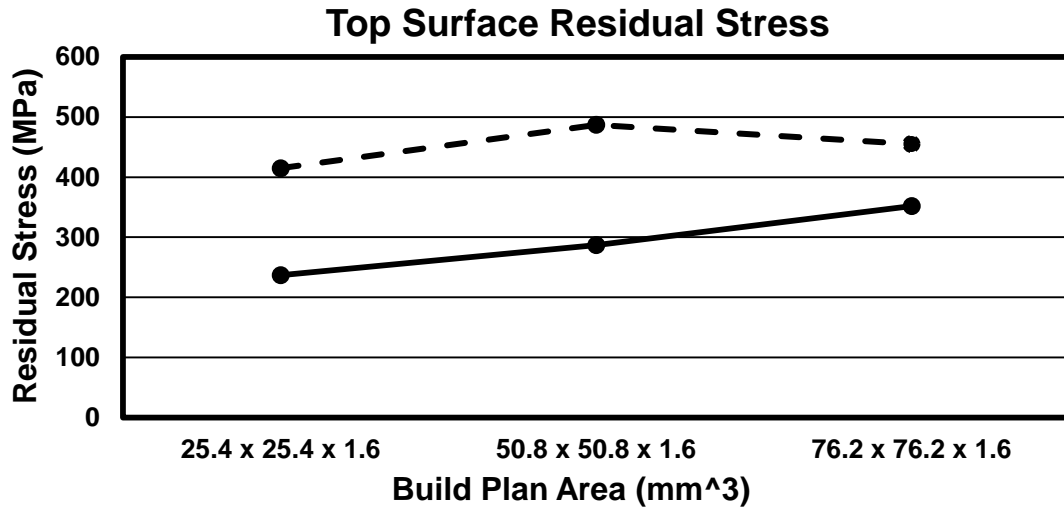
Figure 41: Top surface residual stress measured via XRD on the three different build plan areas

Substrate Bottom Surface Residual Stress
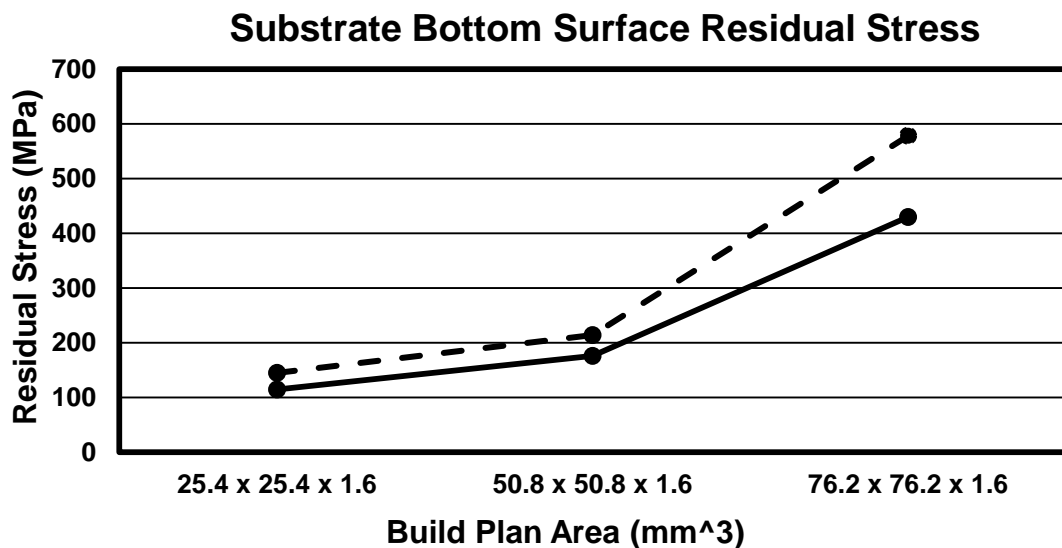
Figure 42: Bottom substrate surface measured residual stress via XRD on the three different build plan areas

In general, the substrate distortion is controlled by the thermal history of the SLM process. During melting, the added material is heated and expands, thus the substrate is forced to distort in the concave down position. Nevertheless, as the material solidifies, the added material contracts, forcing the substrate to distort in the concave up position. For each added layer, the cooling process occurs over a much longer duration than the heating process. Hence, the final

61

distortion of the substrate is generally in the concave up position. Moreover, because hundreds of layers are generally needed for SLM fabrication, the substrate distortion generally increases as build height increases.
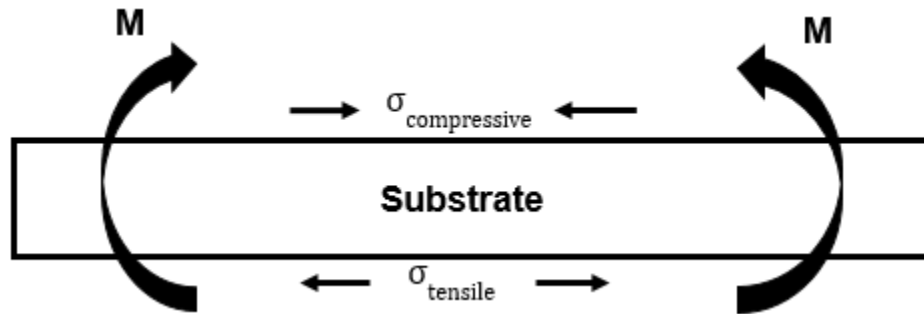
Figure 43: Typical bending moment imposed on the substrate during the SLM process.

As the concave up distortion increases as a function of build height in the substrate, the bottom surface of the substrate is stretched by the bending moment that is created (Figure 43). Thus, the residual stress on the bottom surface of the substrate increases as the distortion increases. The largest out of plane distortion occurred on the substrate with the largest build plane area. Hence, this enabled the largest build plan area to develop the largest substrate bottom surface residual stress.

In prior work, the residual stress developed on the bottom surface of the substrate has often been ignored and not measured. However, controlling and measuring distortion on the bottom surface of the substrate is critical. Ideally, small distortion and limited residual stress development is desired in the SLM process. In this ideal scenario, the substrate remains flat and the deposit maintains desired dimensions throughout the process. Moreover, in this ideal case the development of limited residual stress enables the deposit to be cut from the substrate without distorting. However, this ideal case does not represent

what transpires throughout the SLM process. Figure 44 shows common distortion that occurs when an SLM component is removed from a distorted substrate's surface without being stress relieved. Thus, it is essential to establish methods to reduce the development of build plate residual stress and distortion. Nonetheless, results of this work suggest that reducing build plan area is one method to reduce bottom substrate surface distortion and residual stress.
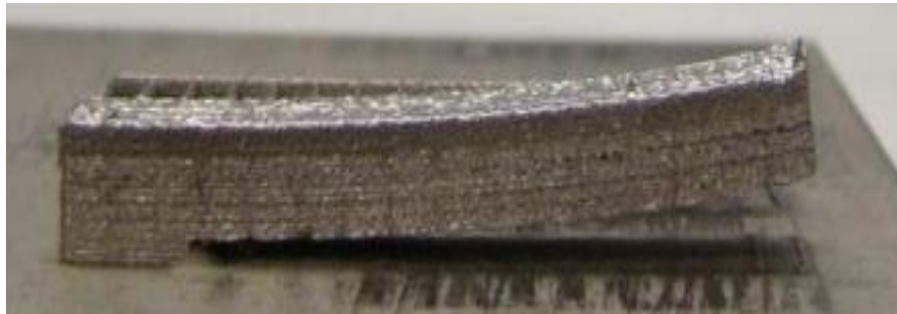
Figure 44: Typical build plate distortion that occurs when a SLM component is removed from its substrate

4.5 Substrate Overhang Results

The residual stress that developed on the top surface of the SLM deposits and the bottom surface of the substrates with and without substrate overhang are shown in Figures 45 and 46. In Figure 45, the measured top surface residual stress of the SLM deposits decreased as build height increased regardless of the substrate size utilized. However, the top surface residual stress was much lower in the deposits that were fabricated on the substrates with no overhang. On the bottom surface of the substrate, the residual stress increased as build height increased for both substrate geometries. However, unlike the top surface residual stress, the residual stress on the bottom surface of the substrate was larger in the substrates with no overhang.
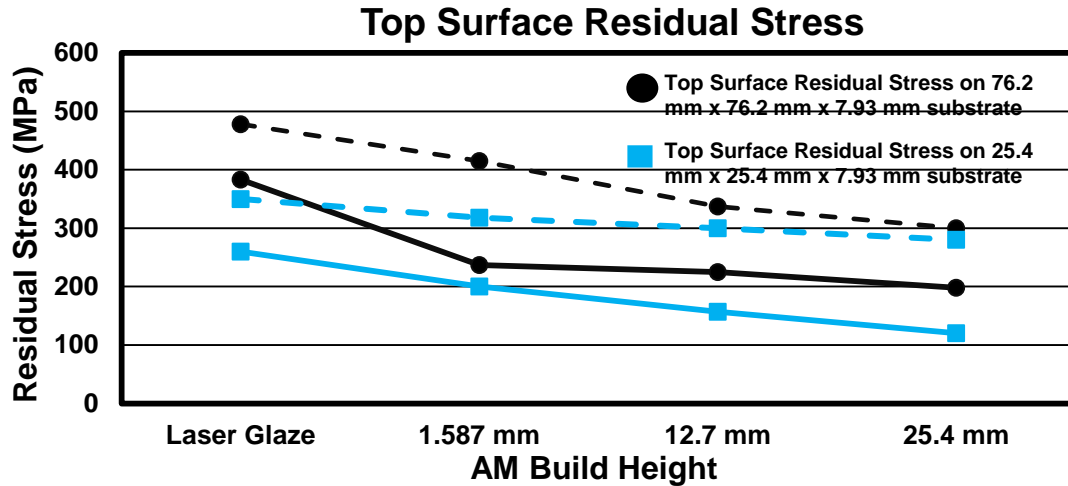
Figure 45: *Top surface residual stress measured via XRD at several build heights. The black lines represent the top surface residual stress measured on the deposit with overhang and the blue lines are the top surface residual stress measured on the SLM deposits that had no overhangs*
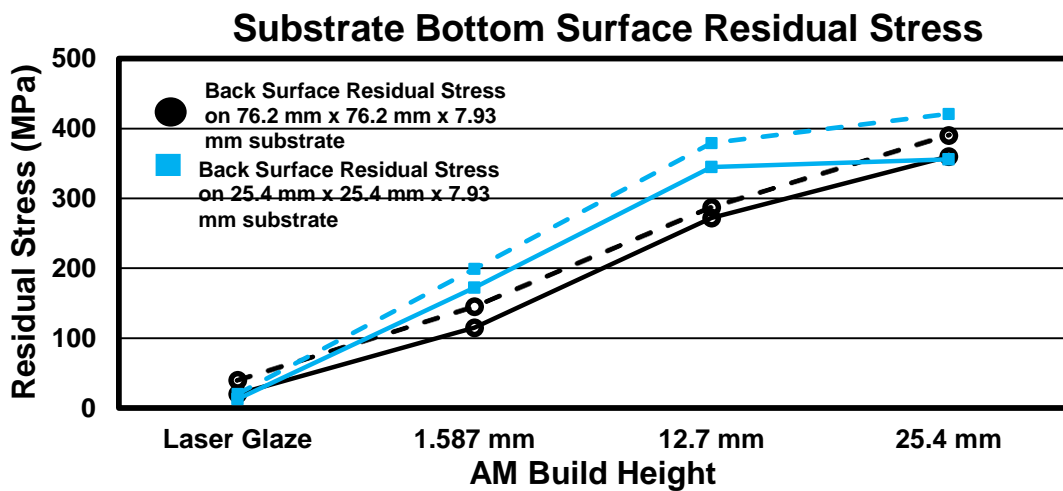
Figure 46: *Bottom substrate surface residual stress measured via XRD at several build heights. The black lines indicate the bottom surface residual stress measured on the deposit with overhang and the blue lines are the bottom surface residual stress measured on the SLM deposits that had no overhangs*

In prior residual stress work on SLM, top surface residual stress at several different build heights (3 mm, 5 mm, and 7 mm) were measured by [49]. Similar to the present work, in [49] it was suggested that top surface residual stress decreased as build height increased. However, contradictory results have been reported by [44]; in which the author's results (at build heights of 2mm, 5mm, and 10 mm) suggested that top surface residual stress increased as a function of

build height. In an attempt to solve the discrepancy in prior works, larger build

heights (3x greater) were fabricated in the present work to further evaluate the

development of top surface residual stress. A likely explanation for the top

surface residual stress trend in Figure 45, is that the SLM deposits experienced

less constraint imposed by the substrate as the build thickness increased. The

first layer of the SLM deposit was fused to the substrate material initially creating

a large bending moment. As material was added, the bulkiness of the deposit

began to oppose the deformation imposed by the substrate, thus lowering the

residual stress development of the top surface of the SLM deposit.

4.6 Scan Speed Results

The top surface residual stress results for the 12.7 mm SLM deposits

fabricated with the three different scan speeds (400, 700, and 1000 mm/s) are

shown in Figure 47. The residual stress on the top surface of the SLM deposit

increased as scan speed increased. Additionally, as shown in Figure 48 the

substrate's back surface residual stress was also influenced by the increase in

scan speed.
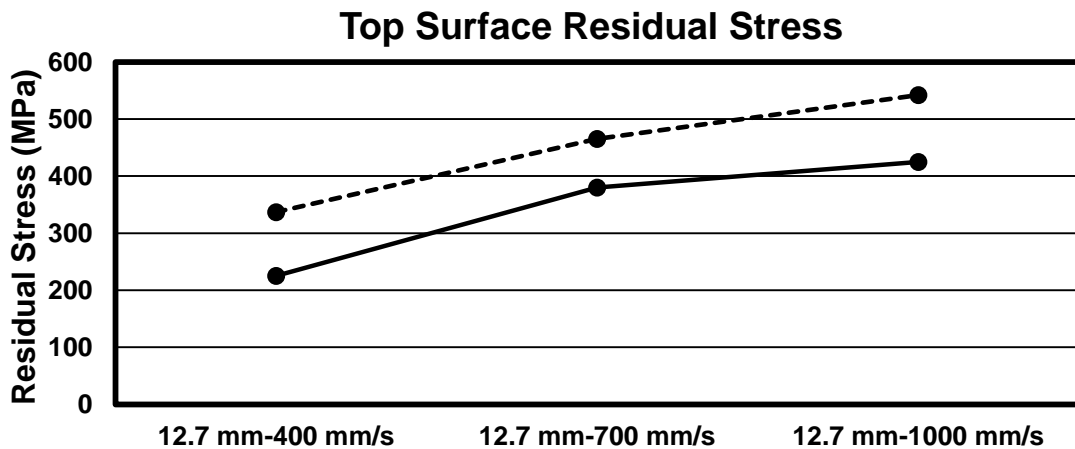
Figure 47: The top surface residual stress measured on the three deposits fabricated with three different scan speeds

Backside Substrate Surface Residual Stress
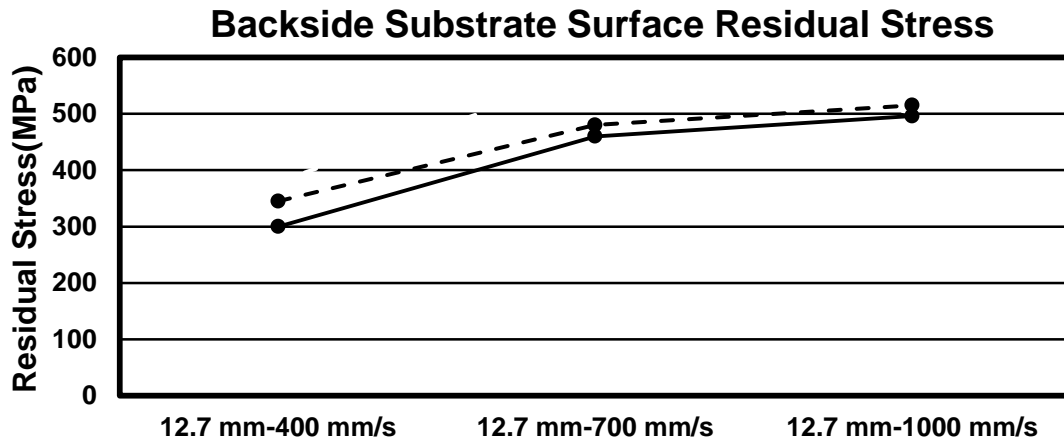
Figure 48: The bottom surface of substrate residual stress measured on the three deposits fabricated with three different scan speeds

4.7 Summary and Discussion of XRD Residual Stress Results

The implementation of XRD was successful in revealing the effect of several process parameters on surface residual stress. By utilizing XRD, process parameters such as laser power, stripe width, scan speed, build height, and build plan area were shown to influence surface residual stress. Perhaps the most novel discovery from these measurements was that several substrate conditions (e.g. substrate overhang and prior stress state) did influence the evolution of residual stress. However, the penetration depth of the x-rays was unfortunately limited to the surface. Therefore, the trends established by XRD on the top surface of the SLM deposits and bottom surface of the substrate were restricted to the surface.

XRD measurements in this work suggested that SLM top surface residual stress was decreased by reducing substrate overhang, decreasing scan speed, increasing laser power, decreasing stripe width, increasing build height and decreasing build plan area. The XRD residual stress measurements revealed that tensile residual stress developed on both the top surface of the SLM deposit

66

and back surface of the substrate. The tensile residual stress that developed on

the top surface of the SLM deposits was induced by the shrinkage of each added

layer, while the tensile residual stress on the bottom surface of the substrate

occurred because of increasing distortion. Also, XRD measurements displayed

that a large directionality existed between the two principal stress directions on

the top surface of the deposit. While residual stress work in SLM is limited, one

notable effort that utilized XRD to measure the top surface residual stress of

various Ti64 cubes was Vrancken et al. [14]. Similar to this work, the author's top

surface results indicated that slower scan speeds and high laser powers

decreased top surface residual stress.

5. HOLE DRILLING RESULTS AND DISCUSSION

5.1 Chapter Overview

In this chapter residual stress measurements obtained via hole drilling are summarized and discussed. The goal of the hole drilling measurements was to verify surface measurements taken by XRD. Moreover, the hole drilling measurements allowed for residual stress to be quantified at depths below the top surface of the SLM deposits and bottom surface of the substrates. Similar to XRD, the hole drilling technique measured σ_{11} and σ_{22} on the top surface of the SLM deposits and bottom surface of the substrates. However, the hole drilling technique was also capable of measuring σ_{22} and σ_{33} on the side surface of the SLM deposit.

In the previous chapter, all XRD measurements were taken on the as-deposited SLM surface and as-received substrate surface. By contrast, for the hole drilling measurements, an EDM was used to remove several mills from the top surface of each SLM deposit. The EDM process generally produces a local tensile stress contaminated layer of < 30 microns. This contaminated layer is deep enough to affect the XRD measurements; however, hole drilling measurements are capable of measuring residual stress well beyond this depth. Therefore, this small contaminated layer did not influence the hole drilling measurements discussed in this chapter.

5.2 Top Surface Hole Drilling Measurements

The results from the top surface hole drilling measurements completed in the center of the SLM deposits are shown in Figures 49-53. In each of these figures,

the first measurement was taken at a depth of 25.4 microns and the deepest measurement was taken at approximately 1 mm. Similar to the XRD measurements, tensile residual stress was measured by hole drilling on the top surface of each SLM deposits. A noticeable directionality in the measurements also occurred throughout the depth of the hole drilling measurements. At several hole drilling depths the maximum principal stress was 2x greater than the minimum principal stress. In addition, the residual stress did not stay constant throughout the depth of the measurements. Instead, the measurements oscillated throughout the hole drilling measurement.
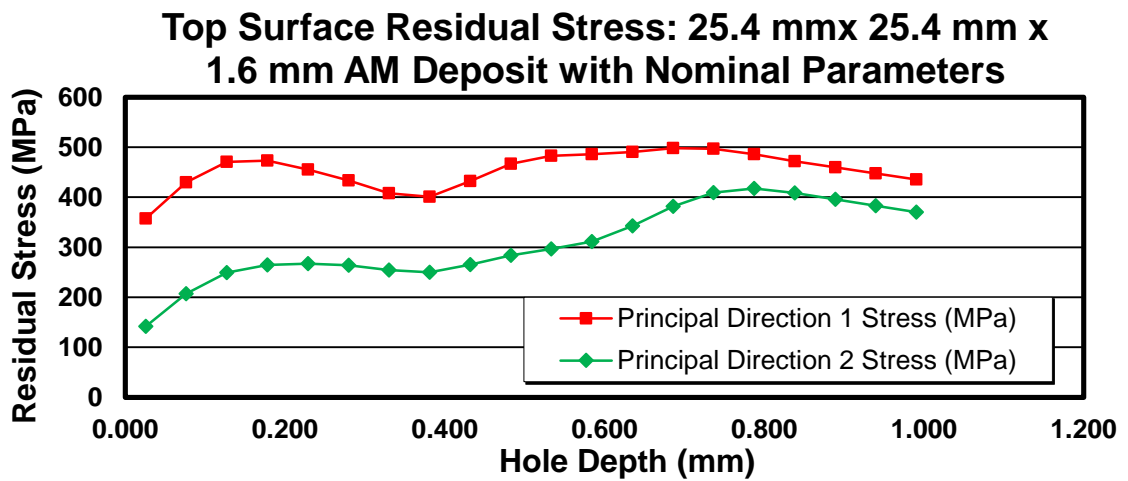
Figure 49: Top surface hole drilling measurements on the 25.4 mm x 25.4 mm x 1.6 mm SLM deposit fabricated with nominal parameters
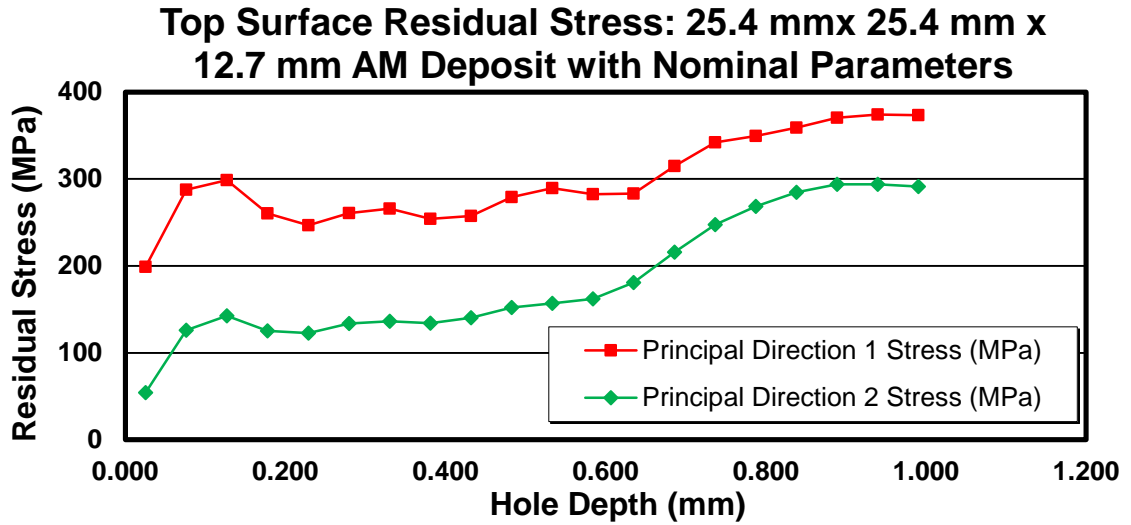
Figure 50: Top surface hole drilling measurements on the 25.4 mm x 25.4 mm x 12.7 mm SLM deposit fabricated with nominal parameters
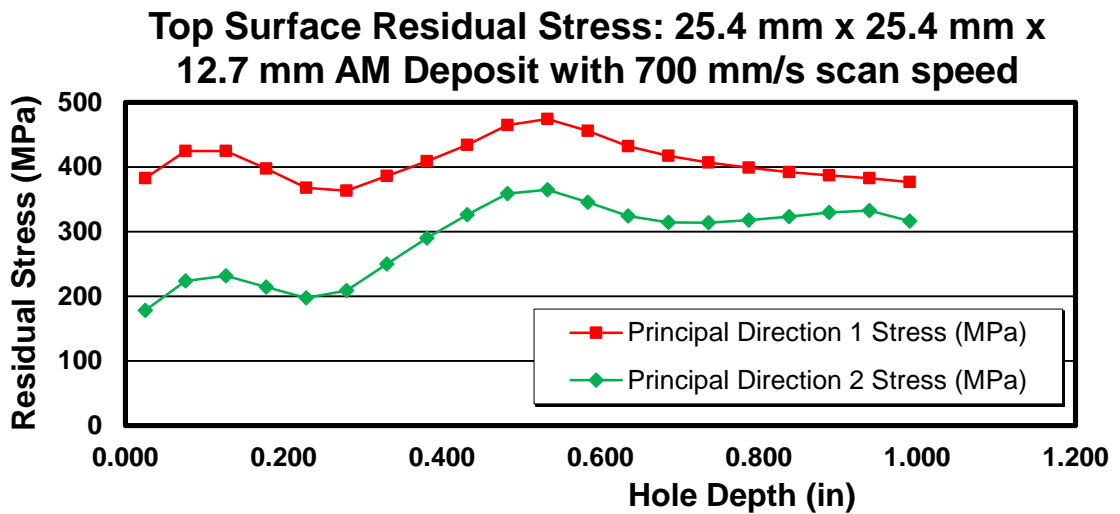
Figure 51: Top surface hole drilling measurements on the 25.4 mm x 25.4 mm x 12.7 mm SLM deposit fabricated with 700 mm/s scan speed

Top Surface Residual Stress: 25.4 mm x 25.4 mm x 12.7 mm AM Deposit with 1000 mm/s scan speed
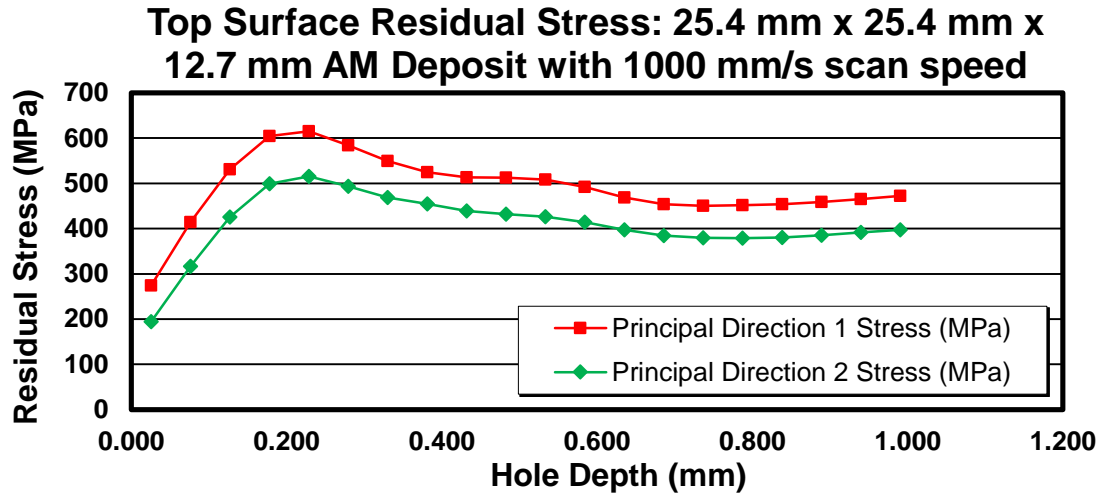
Figure 52: Top surface hole drilling measurements on 25.4 mm x 25.4 mm x 12.7 mm SLM deposit fabricated with 1000 mm/s scan speed

Top Surface Residual Stress: 25.4 mmx 25.4 mm x 25.4 mm AM Deposit with Nominal Parameters
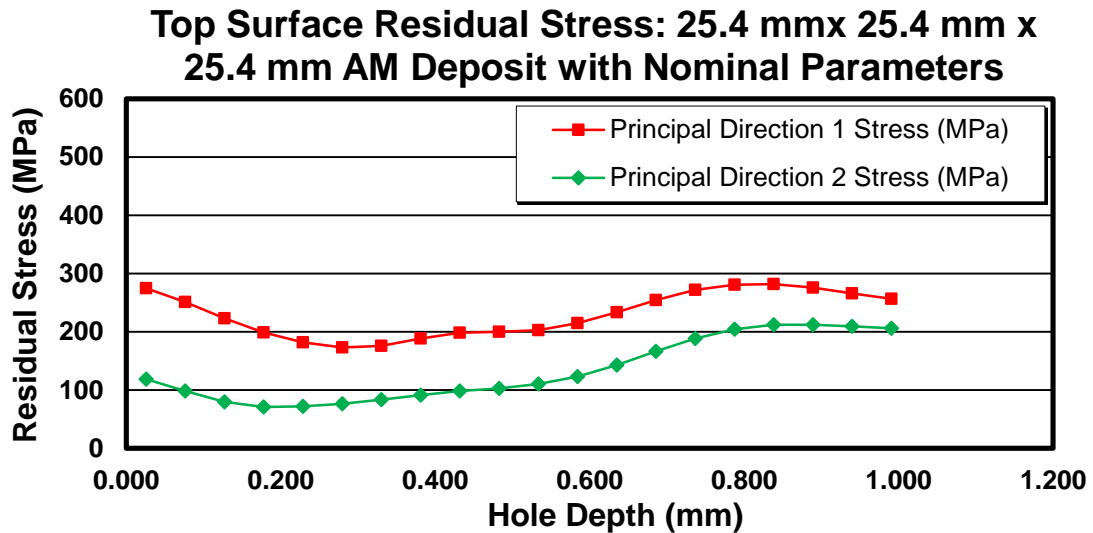
Figure 53: Top surface hole drilling measurements on 25.4 mm x 25.4 mm x 25.4 mm SLM deposit fabricated with nominal parameters

The XRD and hole drilling top surface measurements are compared against one another in Figures 54 and 55. The hole drilling measurement depth used for comparing the two methods was 76.2 microns which resided below the contaminated EDM layer.

In Figure 54, the deposit's top surface residual stress measured by both methods exhibited similar trends. In this regard, the maximum principal stresses

71

measured by XRD and hole drilling were relatively close, agreeing within 20 percent of one another. On the other hand, the minimum principal stresses measured by XRD and hole drilling were drastically different at the build heights of 12.7 mm and 25.4 mm. Likewise, the hole drilling and XRD residual stress measurements completed on the top surface of the three different scan speed fabrications (in Figure 55) show similar trends. However, the hole drilling measurements were once again lower in magnitude when compared to the XRD measurements. Because of this discrepancy, hole drilling measurements were taken on the bottom surface of the substrate to further compare the techniques.
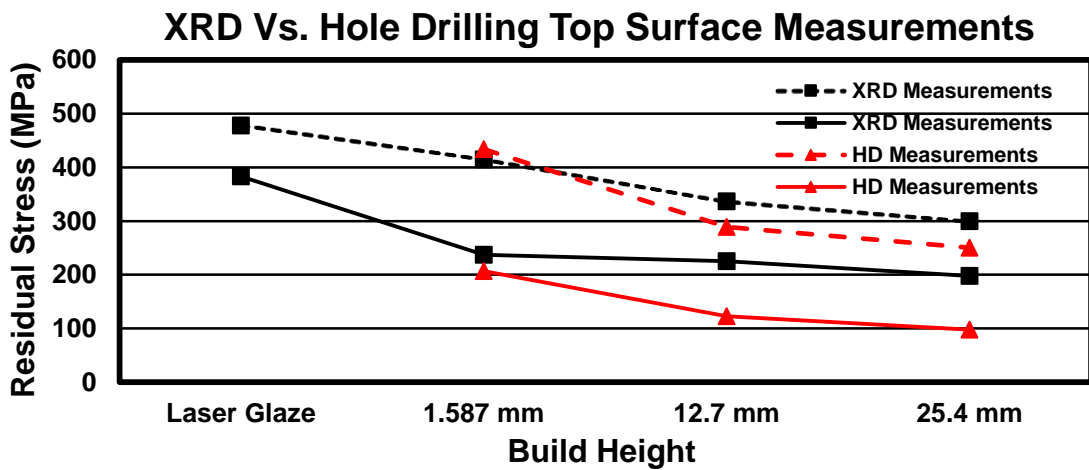
Figure 54: XRD and hole drilling top surface residual stress measurements for different build heights.

XRD Vs. Hole Drilling Top Surface Measurements
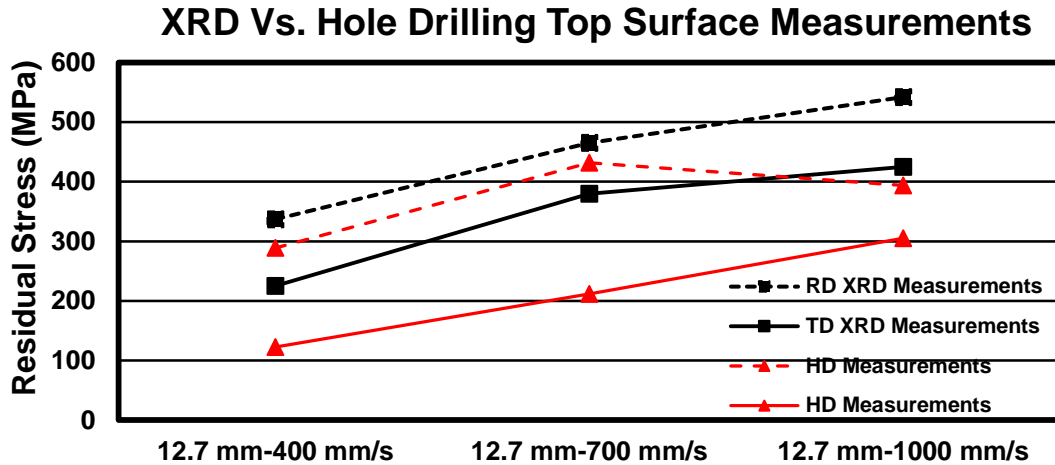
Figure 55: XRD and hole drilling top surface residual stress measurements on the SLM builds fabricated with different scan speeds.

The trends established on the top surface of the AM deposits also continued throughout the thickness of the hole drilling measurements (Tables 3 & 4). In this regard, the residual stress measured at three different hole drilling depths continued to maintain the following two surface established trends: residual stress increased as build height increased and residual stress increased as scan speed increased.Thus, these trends suggested that process parameters affect the development of residual stress on the surface and throughout the bulk of the SLM deposit.

Hole Drilling Measurements at Several Depths: Nominal Parameters

Hole Depth (mm)	1.6 mm Build σ_{11} (MPa)	1.6 mm Build σ_{22} (MPa)	12.7 mm Build σ_{11} (MPa)	12.7 mm Build σ_{22} (MPa)	25.4 mm Build σ_{11} (MPa)	25.4 mm Build σ_{22} (MPa)
0.0762	426.9	207	287.0	126	251	98
0.2794	433.5	264	261	133	176	83
0.5334	483	297	289	156	202	110

Table 3: Top surface hole drilling measurements taken at several depths completed on the deposits with different build heights

Hole Drilling Measurements at Several Depths: Different Scan Speeds

Hole Depth (mm)	12.7 mm Build: Nominal σ_{11} (MPa)	12.7 mm Build: Nominal σ_{22} (MPa)	12.7 mm Build: 700 mm/s σ_{11} (MPa)	12.7 mm Build: 700 mm/s σ_{22} (MPa)	12.7 mm Build: 1000 mm/s σ_{11} (MPa) :	12.7 mm Build: 1000 mm/s σ_{22} (MPa)
0.0762	287.0	126	425	208	414	316
0.2794	261	133	386	250	549	468
0.5334	289	156	474	365	461	426

Table 4: Top surface hole drilling measurements taken at several depths completed on the deposits fabricated with different scan speeds

5.3 Back Surface Hole Drilling Measurements

Unlike the top surface of the SLM deposit, the back of the substrate did not need to be machined for the hole drilling measurements. Therefore, the first measured hole drilling depth was chosen for comparing the XRD and hole drilling. Surprisingly, on the bottom surface of the substrate the hole drilling measurements were *higher* than the XRD measurements (Figures 56 & 57). Also, unlike the top surface of the deposit, the XRD and hole drilling measurements on the bottom substrate surface were within 20 percent of one another. Furthermore, both residual stress techniques measured a smaller directionality between the principal stresses on the bottom surface of the substrat
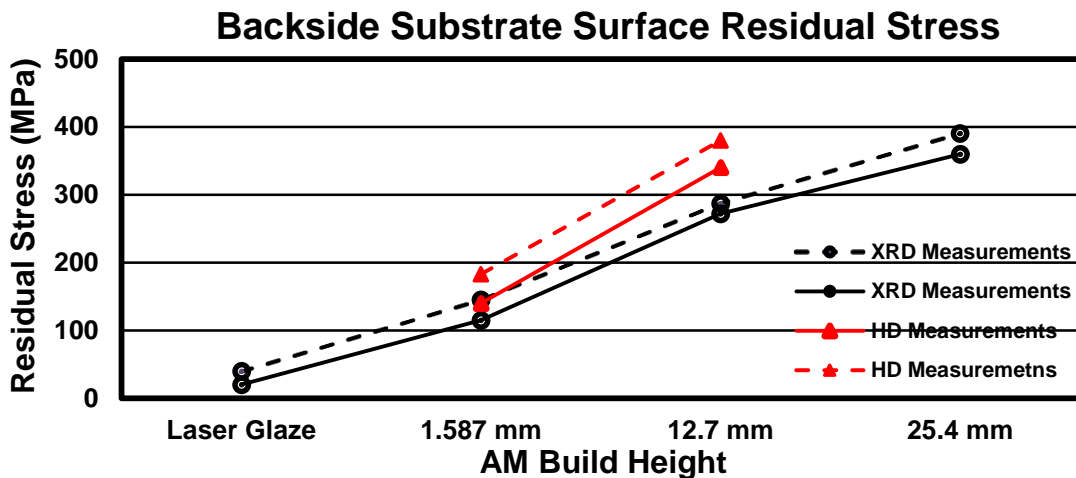
Figure 56: XRD and hole drilling measurements performed on the bottom surfaces of the substrates

Backside Substrate Surface Residual Stress
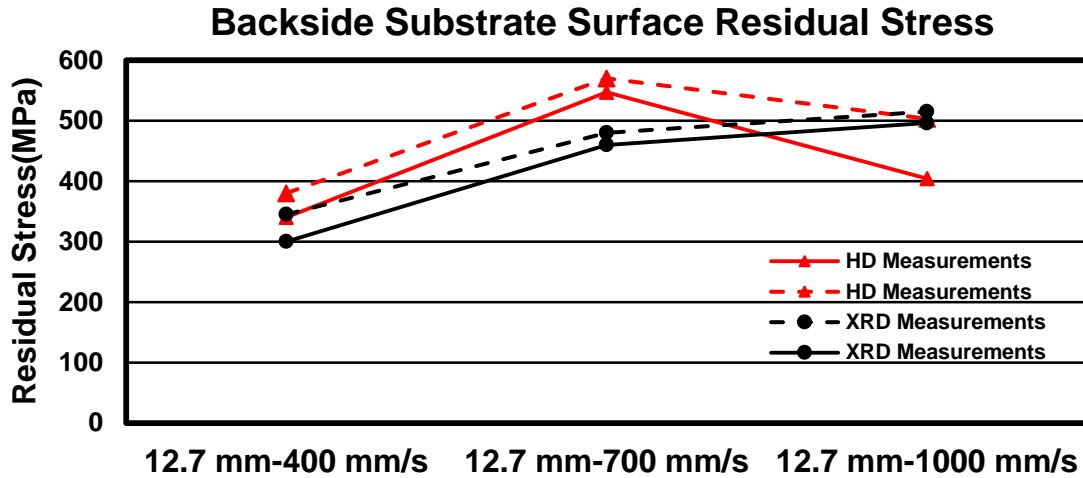
Figure 57: XRD and hole drilling measurements performed on the bottom surfaces of the substrates

5.4 Side Surface Hole Drilling Measurements

Hole drilling measurements were also implemented on side surface of the largest SLM deposit (25.4 mm x 25.4 mm x 25.4 mm). On the side surface of the SLM deposit, σ_{22} and σ_{33} were measured, and the measurement results are shown in Figure 58. The blue lines in Figure 58 correspond to the hole drilling measurement taken at a build height of 19.05 mm on the side surface. The red lines denote the side surface hole drilling measurement taken at a build height of 6.35 mm. Similar to the top surface of the AM deposit, the residual stress was nonuniform throughout the depth of the hole drilling measurement and a large directionality existed between the two measured principal directions.

Side Surface Residual Stress: 25.4 mmx 25.4 mm x 25.4 mm AM Deposit with Nominal Parameters
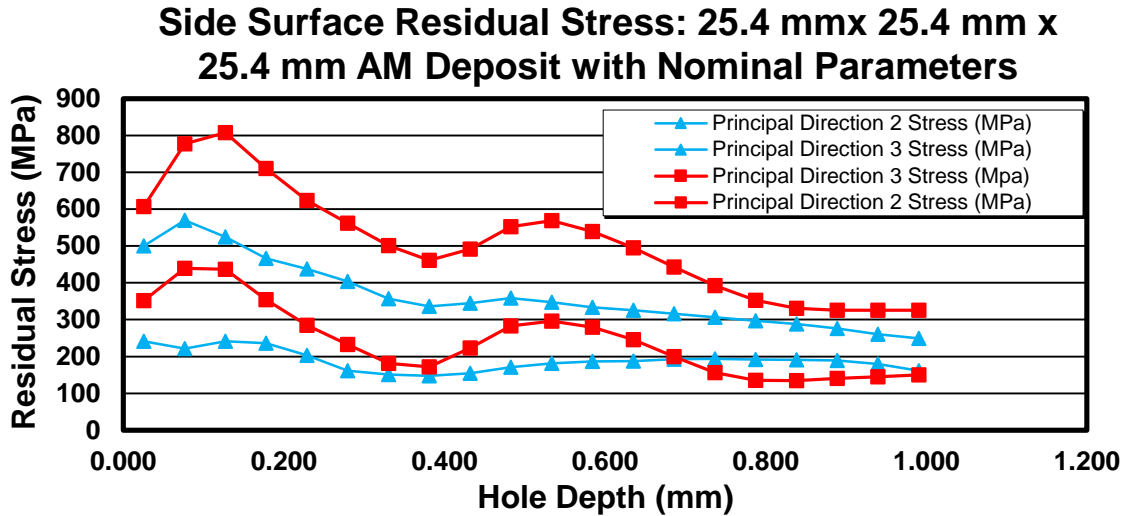
Figure 58: Side surface hole drilling measurements on the largest SLM deposit. The red lines represent the hole drilling measurements taken at a height of 6.35 mm and the blue lines represent the residual stress measured at a build height of 19.05 mm on the side surface.

5.5 Summary and Discussion of Surface Residual Stress Results

In prior residual stress work, typically one experimental method was utilized to measure residual stress. Limited literature exists on comparing multiple residual stress techniques to measure the same region of interest. One notable attempt to measure residual stress by XRD and hole drilling in the same location was undertaken by Ceglias et al [62]. In Ceglias's work, similar trends were established by both measurement techniques. However, the two measurement techniques measured very different magnitudes of residual stress. Specifically, the XRD measurements in Ceglias's work were typically much greater than the hole drilling measurements taken in the same locations. In the present work, XRD and hole drilling measured comparable residual stress in Figures 56 and 57. Yet, XRD and hole drilling measurements were drastically different in Figures 54 and 55. Thus, it is important to understand possible reasons for these discrepancies.

76

Perhaps one of the most important parameters used for XRD measurements is the X-ray Elastic Constant (XEC). The XEC varies for a specified hkl plane and in each material. For instance, the XEC for the (21.3) hkl plane for pure Titanium, Ti-6Al-4V, and Ti-6Ai-2Sn-4Zr-2MO is 90.3 GPa, 84.1 GPa, and 102 GPa respectively [43]. Although each of the three materials is a Titanium alloy, the XEC for each material is very different. Moreover, errors can arise in XRD measurements when incorrect XEC's are utilized.

The XEC used for this work was specified by [43] as the correct XEC for Ti64. However, different preferred crystallographic textures can influence the XEC of the material. In this regard, the crystallographic texture in the SLM builds and substrate material could have caused errors in the XRD measurements. Furthermore, errors in the XRD measurements could have also occurred from defects present on the as-fabricated SLM surfaces. These surface defects include: unmelted powder particles attached to the surface, surface roughness, and surface cracks created by the utilized scan strategy.

6. CONTOUR AND LAYER REMOVAL RESULTS AND DISCUSSION

6.1 Chapter Overview

Similar to the surfaces of the deposit, two residual stress techniques were utilized to measure the residual stress throughout the bulk of the SLM deposits. In this regard, the layer removal and contour methods were utilized for the measurements. In particular, the contour technique utilized in this work measured the residual stress in the rolling direction that aligned closely with σ_{11}. The layer removal method measured the residual stress in the rolling and transverse direction at several instantaneous heights. Furthermore, the contour method was implemented on SLM deposits with and without substrate overhang. The layer removal method was only applied on SLM deposits with no substrate overhang.

6.2 Layer Removal Measurements

The layer removal results from the 14.7 mm thick SLM deposit are shown in Figure 59. Ten slices were taken for the measurements. Upon inspection of the results, a tensile region existed near the top surface of the SLM deposit and was balanced by a compression region in the middle. The compression region occurred for approximately 8 mm and was replaced by tensile residual stress near the substrate and SLM material interface. The residual stress measured in the rolling and transverse direction at each instantaneous height displayed similar trends and magnitudes. In addition, there was no large directionality between the two measured directions. Unfortunately, the results in Figure 59 did not maintain force and moment equilibrium. Because of this, the layer removal

technique was implemented on an additional 25.4 mm x 25.4 mm x 25.4 mm

deposit fabricated on a substrate with no overhang.
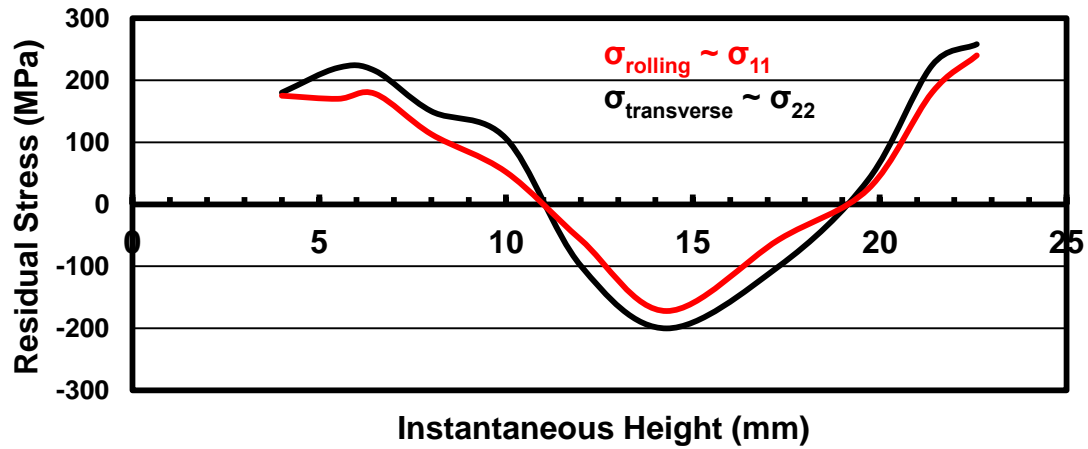
Figure 59: 14.7 thick SLM deposit layer removal results

In order to better understand the layer removal data, a *smaller* average slice

thickness was utilized on the second deposit. In total 38 slices of material were

removed from the 25.4 thick deposit. When the layer removal procedure was

complete, only the substrate material was left. Noticeably, the results in Figure 60

displayed good force and moment balance. One possible reason for the better

force and moment balancing was the reduction in slice thickness. In this regard,

Equation 11 and 12 indicate that the residual stress is dependent on the slope

profile at each instantaneous height. The slopes of the strain measurements at

each instantaneous height must be smoothed in order to be accurately applied to

Equation 11 and 12. By increasing the number of slices in the layer removal

process, the strain measurements can be more accurately smoothed and thus,

the residual stress can be calculated more accurately.
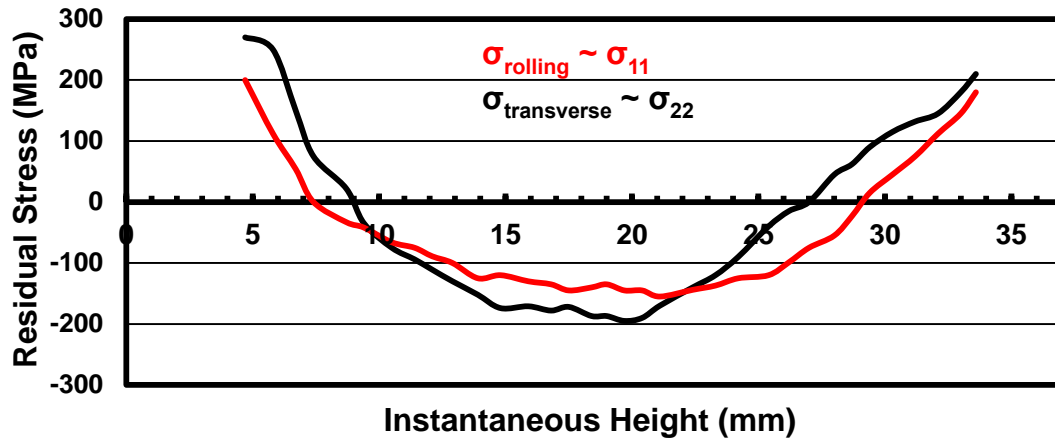
Figure 60: 25.4 thick SLM deposit layer removal results

One additional layer removal experiment was completed on a 25.4 mm x

25.4 mm x 25.4 mm cube that was stress relieved prior to the slicing operation.

Similar to the two SLM deposits, several slices were removed from the sample

until the height of the cube was 5 mm. The strain measured by the strain gauges

was not affected after each cut and remained close to zero throughout the slicing

operation. Traditionally an EDM or chemical etchant is used to remove material

during the layer removal procedure. However, the results obtained from the

stress relieved sample suggested that a low abrasive saw is also suitable for this

procedure.

6.3 Contour Measurements

The contour results obtained from the SLM deposit fabricated on the

substrate with no overhang are shown in Figure 61. The three lines denoted in

Figure 61 were the three locations at which residual stress was plotted. The

black line represented the residual stress measured across the mid width of the

SLM deposit and substrate. The purple line represented the residual stress

measured through the mid thickness of the substrate. Finally, the red line

represented the residual stress measured throughout the mid thickness of the

SLM deposit (Figures 62-64).

Figure 61: Contour measurement results from the 25.4 mm x 25.4 mm x 25.4 mm SLM deposit with no substrate overhang

Figure 62: Mid width contour measurements

Mid Thickness of AM Deposit

Figure 63: Mid thickness of SLM deposit measurements

Mid Thickness of Substrate
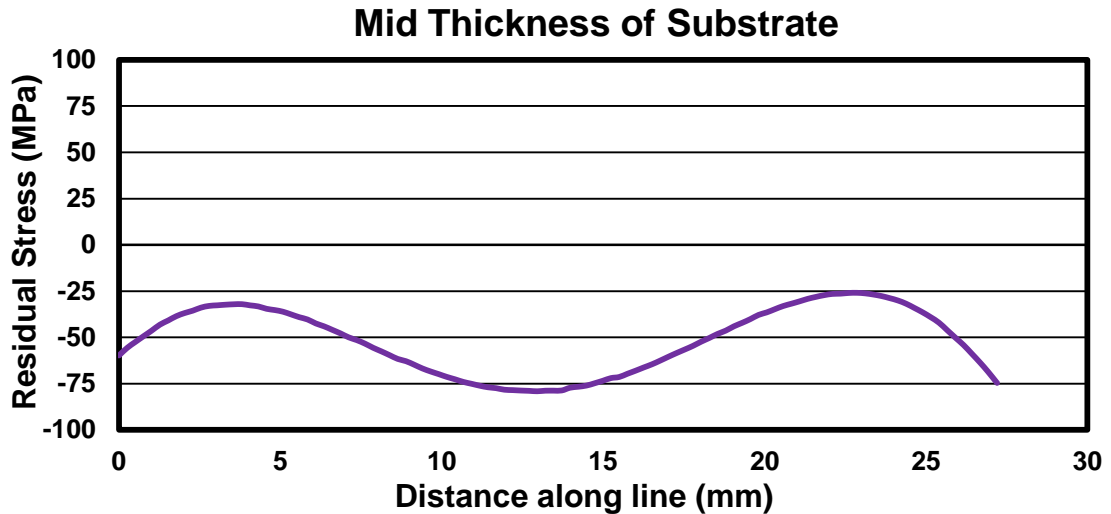
Figure 64: Mid thickness of the substrate measurements

The contour measurement completed on the SLM deposits with substrate overhang is shown in Figure 65. In comparing both of the contour measurements, the residual stress throughout the bulk regions were extremely different. Strikingly, the top surface and side surface residual stress measured on the deposit with substrate overhang was much larger, when compared to the deposit with no overhang. Furthermore, while both deposits had large tensile regions on the bottom surface of their attached substrate, the compression region was much greater in the deposit fabricated on the substrate with

overhang. In addition, both contour maps measured tensile residual stress on the side surfaces and top surface of the SLM deposit, qualitatively corroborating the previous XRD and hole hole drilling measurements. Yet, the largest inaccuracy of the contour measurements is near the surfaces of the sectioned plane and therefore, the contour measurements cannot be directly compared to the XRD and hole drilling measurements.
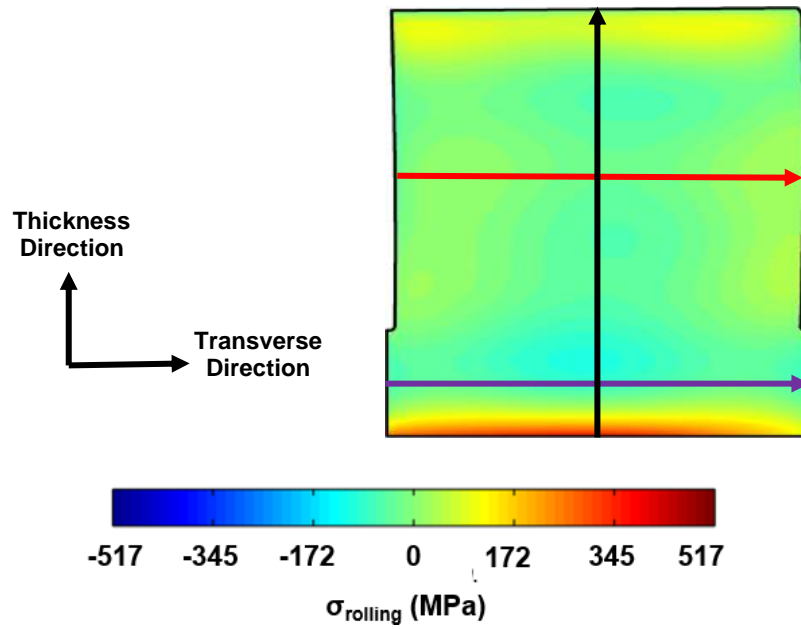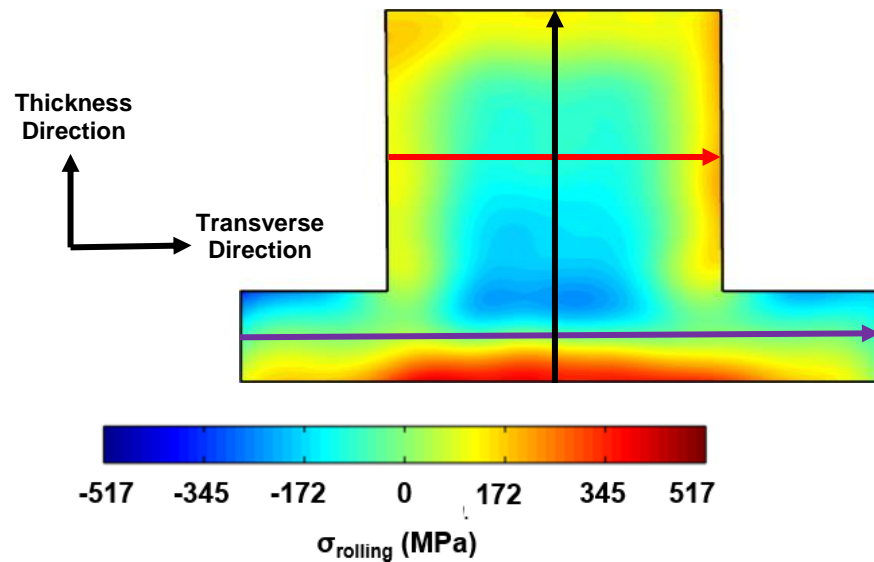

Figure 65: Contour measurement results from the 25.4 mm x 25.4 mm x 25.4 mm SLM deposit with substrate overhang

Mid Width of Contour Measurement
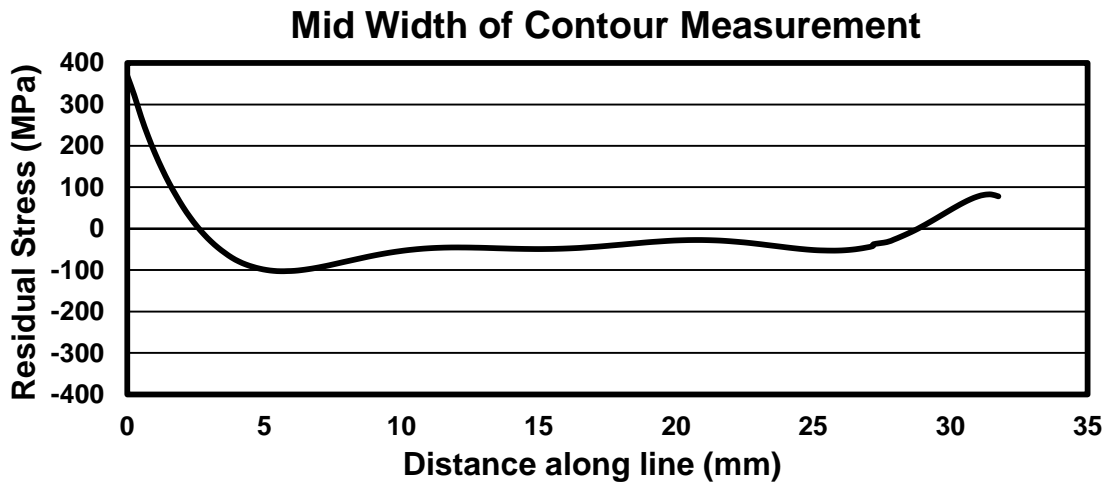

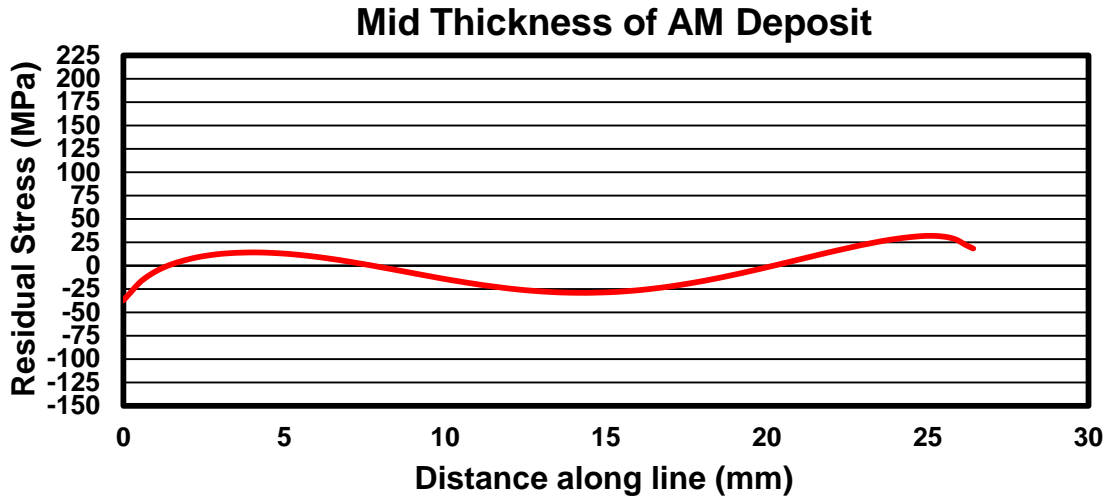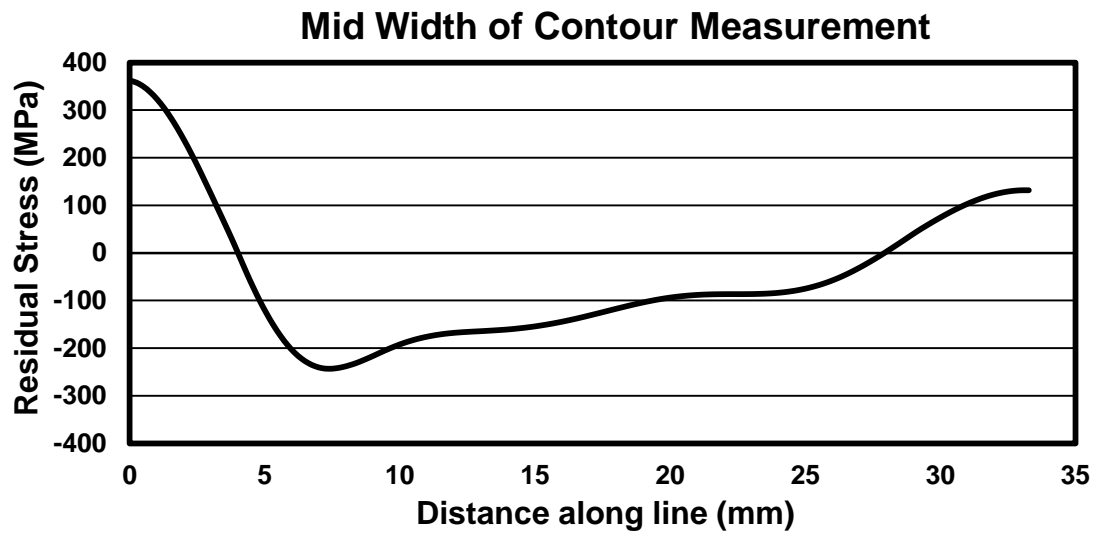*Figure 66: Mid width contour measurements*

Mid Thickness of AM Depsoit
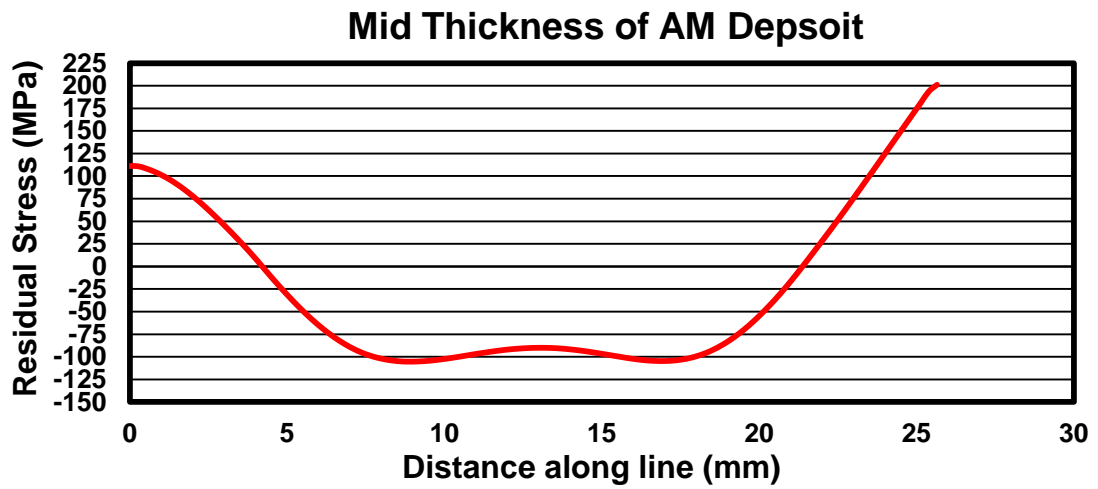
Figure 67: Mid thickness of the SLM deposit measurements

Mid Thickness of Substrate
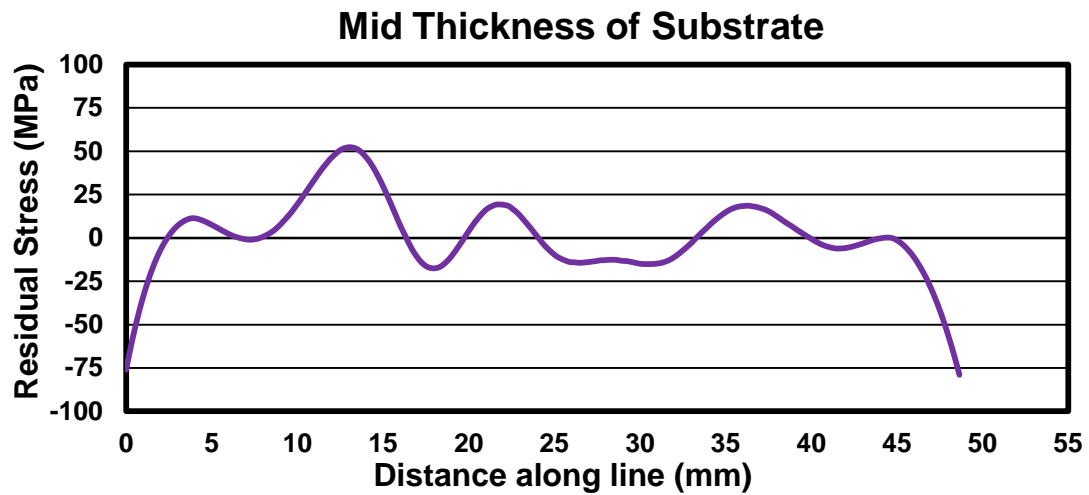
Figure 68: Mid thickness of the substrate measurements

The layer removal and contour method were both completed on the 25.4 mm

x 25.4 mm x 25.4 mm deposit fabricated on the substrate with no overhang. Both

of the techniques measured residual stress throughout the bulk of the component

in the rolling direction. Therefore, the two methods are compared in Figure 69. As

shown in Figure 69, the layer removal and contour measurements exhibited

similar trends. However, there were differences in the measured magnitudes.

Yet, the difference in the measurements may have occurred because each

technique measures residual stress differently.
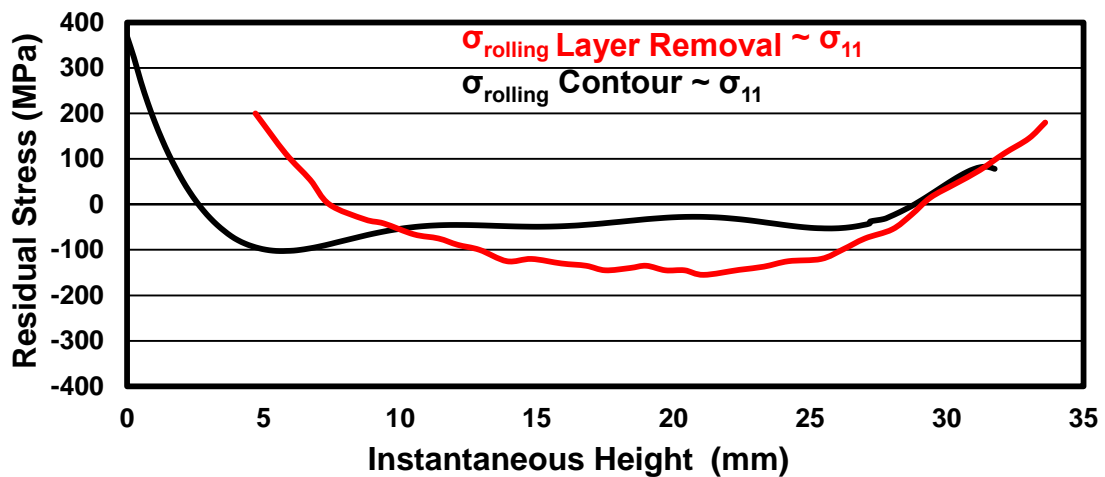
Figure 69: Comparing contour and layer removal measurements taken in the rolling direction

6.4 Summary of Bulk Results and Discussion

The results obtained and discussed in this section helped establish residual stress trends throughout the depth of the SLM deposit. XRD, hole drilling, layer removal, and contour measurements established that tensile residual stress develops on the top surface of the SLM deposit and bottom surface of the substrate. The hole drilling and the contour measurements also showed that tensile residual stress develops on the side surfaces of the SLM deposit. Also, the results in this chapter established that compressive residual stress develops throughout the bulk of the SLM component. Furthermore, the two contour measurements also suggested that residual stress throughout the SLM deposit can be reduced if a substrate with no overhang is utilized.

Similar to XRD, Vrancken et al. also performed contour measurements on several Ti64 SLM deposits [14]. One of the author's contour measurements is shown in Figure 70. Specifically, Vrancken's contour measurement was done throughout the thickness of the SLM deposit after the deposit was machined from the substrate. As the SLM deposit was cut from the substrate surface, the residual stresses redistributed themselves to maintain equilibrium. Thus, the residual stress in Figure 70 does not represent the initial residual stress developed in the SLM deposit. In Vrancken's measurements, tensile residual stress was measured at the interface between the substrate and SLM material and at the SLM deposit's top surface. Moreover, the measured residual stress was compressive in the bulk of Vrancken's deposit. For this work, the SLM deposits were left on their respective substrates for the contour measurements.

Similar to Vrancken's measurements, the contour measurement in this work

showed tensile residual stress developed on the top surface of the SLM deposit.

Yet, the substrate and SLM material interface was in compression because the

component remained on the substrate. In addition, the residual stress on the

bottom surface of the substrate was tensile enabling force balancing of the

component. This side by side examination shows that residual stress in SLM

deposit is redistributed when it is removed from the substrate. Therefore, in order

to measure the true residual stress induced by the SLM process, the SLM

deposit must remain on its respective substrate.
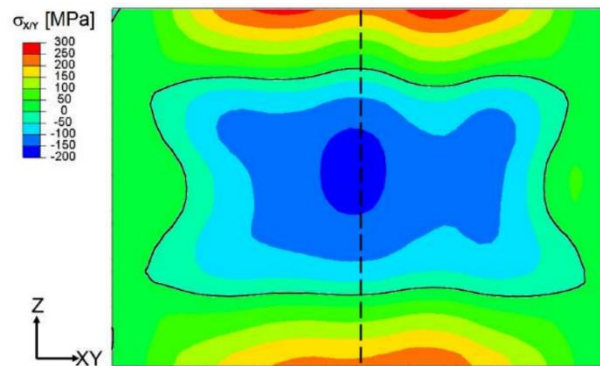
Figure 70: Vrancken's contour measurement made through the thickness of the SLM deposit. The deposit was machined off its substrate prior to the measurement [14]

7. CONTRIBUTIONS

The contributions in this thesis include:

1. Established the effect of several process parameters (laser power, stripe width, scan speed, substrate overhang, build height, substrate condition, and build plan area) on top surface residual stress

2. Established the effect of scan speed, substrate overhang, and build plan area on bottom substrate surface residual stress

3. Established residual stress development in SLM utilizing several measurement techniques (e.g. XRD, hole drilling, layer removal, and contour)

8. FUTURE WORK

The work discussed in this thesis has demonstrated the effect of process parameters on surface and bulk residual stress. However, several aspects need to be further investigated and include:

1) Modeling of the results obtained and repeated experimental studies of work done in this thesis

2) Establishing the effect of additional SLM process parameters on residual stress to further understand methods to reduce and control its development throughout the process

3) Determining the specific XEC for stress relieved Ti64 substrates and additively manufactured Ti64 in attempt to solve the discrepancy in the XRD and hole drilling measurements

4) Microstructure and texture analysis to further understand if it impacts the development of residual stress or vice versa

In reference to 4), a preliminary microstructure and texture analysis were undertaken. The goal of the analysis was to determine if residual stress in the regions could be explained by a change in microstructure. The BSE images taken in the specified locations (discussed in section 3.6) are shown in Figure 71. The microstructure at the top surface and mid height of the deposit developed a very fine martensitic α phase. Thus, the material in both regions experienced temperatures above the beta transus and cooled very quickly. The microstructure of the bottom surface of the substrate contained equaixed α particles that were developed during the initial stress relieving of the substrate. Moreover, the

microstructure on the bottom surface of the substrate remained unchanged during the SLM fabrication process.

As previously mentioned, the contour and layer removal method measured tensile residual stress on the top surface of the SLM deposit. The microstructure in the top region of the SLM deposit suggested a fast cooling rate and high thermal gradients occurred and therefore, the development of tensile residual stress was expected. Hence, the microstructure is in agreement with the developed residual stress. However, this was not the case in the mid height of the SLM deposit or bottom substrate surface. In this regard, the same martensitic microstructure was present at the mid height of the SLM deposit indicating that the material was rapidly cooled. However, the residual stress in this region was compressive and therefore, the microstructure is not in agreement with the developed residual stress. Furthermore, the microstructure of the bottom surface of the substrate contained equaixed alpha particles. This microstructure suggested that the material was cooled slowly and therefore, the residual stress was expected to be small. Yet, the residual stress in the bottom surface of the substrate was highly tensile. Thus, while the microstructure can explain the residual stress development in one instance, it fails to do so in other instances.
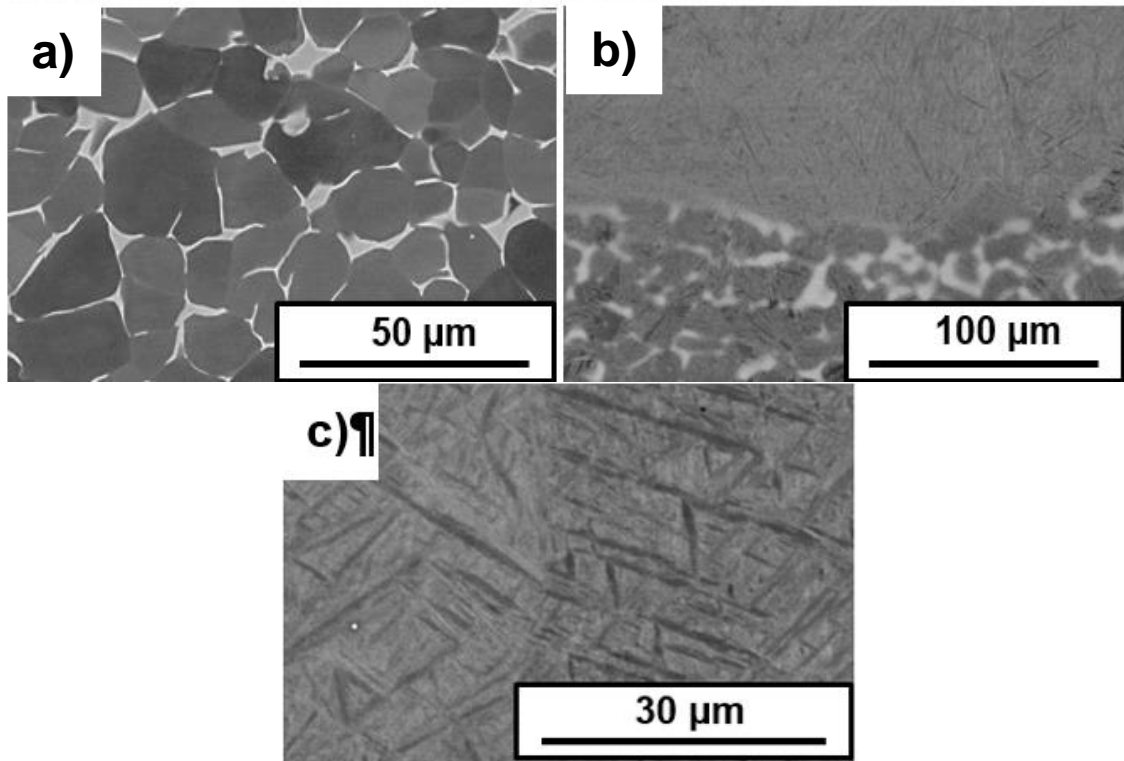
Figure 71: BSE images showing the microstructure of several locations denoted in Section 3.6: a) is the microstructure of the bottom surface of the substrate, b) is the microstructure of the SLM material and substrate interface, and c) is the microstructure of the top of the SLM deposit

The EBSD montage of location 1 is shown in Figure 72. The substrate

material extended approximately 1 mm to the left of the right edge of the

montage. The SLM build thickness captured in the montage was approximately 6

mm. In order to better assess the crystallographic texture as a function of build

height, three regions were cropped from the EBSD montage. These areas

included: a region containing only substrate material, a region at a build location

of 3 mm, and a region at build location of 6 mm. The cropped regions are shown

in Figure 73. Moreover, the 3 PF for each cropped region are shown in Figure 74.

In Figure 74, the crystallographic texture of the substrate and SLM material was

very different. By contrast, the crystallographic texture of the two different build

locations was relatively similar. Thus, it is likely that crystallographic texture does

not change throughout the build thickness. Therefore, it is likely that residual stress does not influence texture evolution.
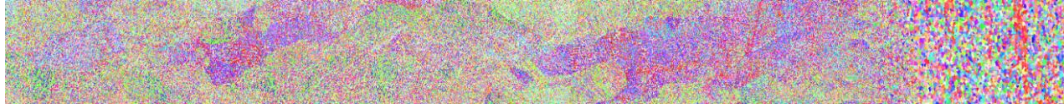
Figure 72: EBSD Montage of location 1
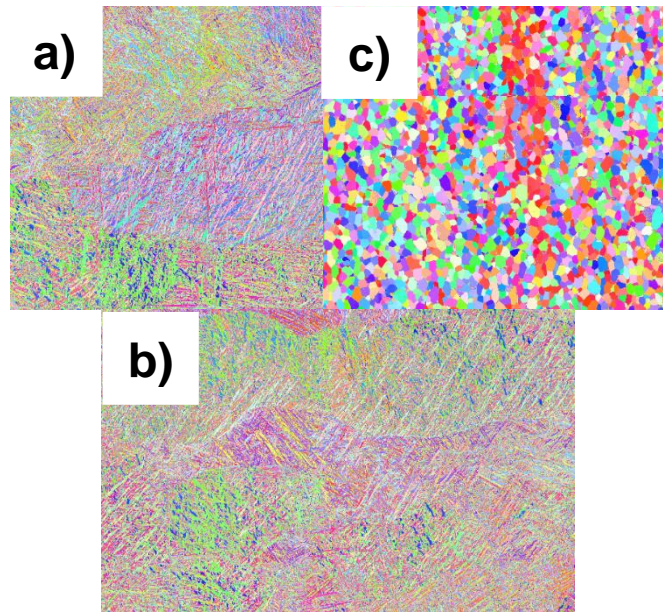
Figure 73: Cropped EBSD regions: a) cropped region at a build location of 6 mm, b) cropped region at a build location of 3 mm, and c) cropped substrate region
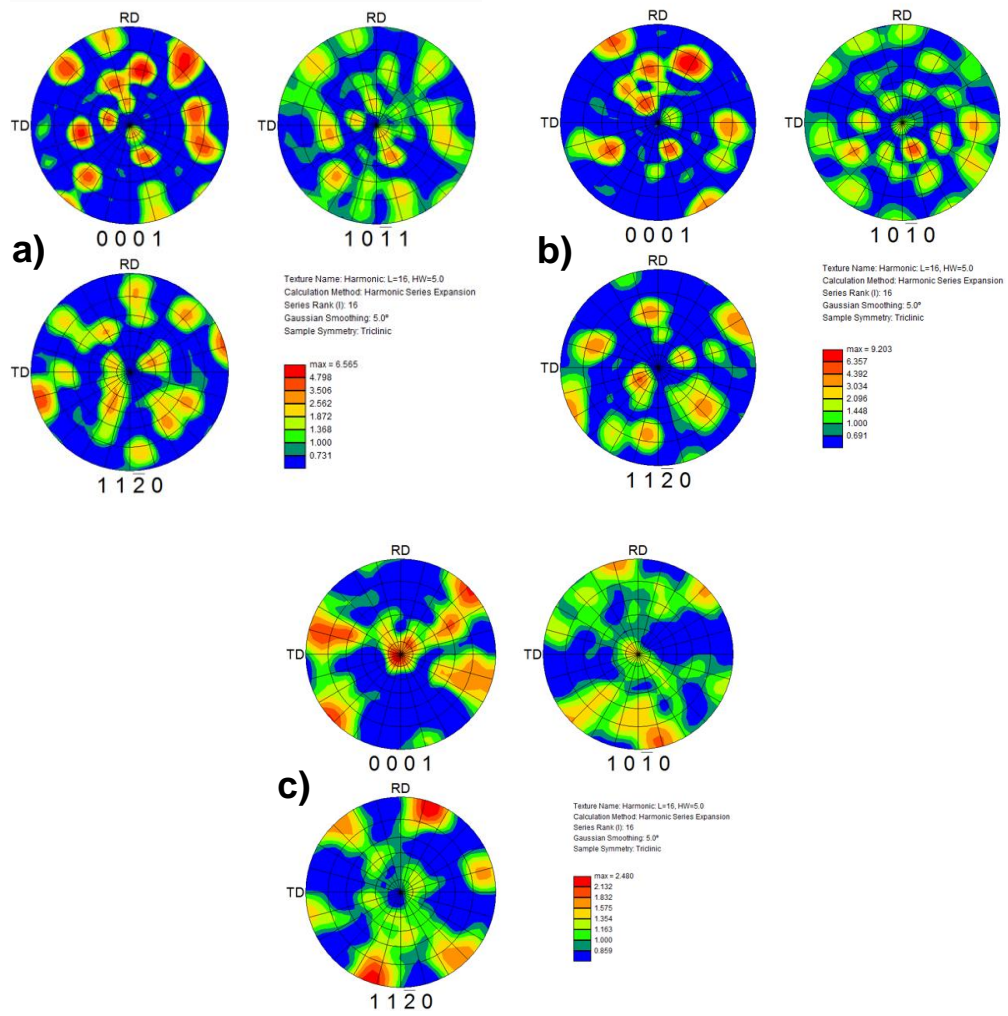
Figure 74: PF of the cropped regions: a) PF at a build location of 6 mm, b) PF at a build location of 3 mm, and c) PF of substrate region

9. CONCLUSIONS

The work in this thesis has experimentally established the effect of many process parameters on residual stress in SLM Ti64. It was shown in this work that process parameters influence the development of residual stress on the surfaces and in the bulk of SLM deposits. Moreover, it is likely that the residual stress trends established in this thesis will also exist in the SLM of other material systems. Thus, the experimental results in this thesis have enabled a pathway for future residual stress modeling efforts in the SLM of various materials. Furthermore, this thesis was successful in establishing an experimental methodology to control and reduce the evolution of unwanted residual stress in SLM builds.

WORKS CITED

[1] P. A. Kobryn and S. L. Semiatin, "The laser additive manufacture of Ti-6Al-4V," *JOM*, vol. 53, no. 9, pp. 40–42, 2001.

[2] K. Wong and A. Hernandez, "A review of additive manufacturing," *ISRN Mechanical Engineering*, 2012.

[3] S. H. Huang, P. Liu, A. Mokasdar, and L. Hou, "Additive manufacturing and its societal impact: a literature review," *The International Journal of Advanced Manufacturing Technology*, vol. 67, no. 5-8, pp. 1191–1203, 2012

[4] B. Baufeld, O. V. D. Biest, and R. Gault, "Additive manufacturing of Ti–6Al–4V components by shaped metal deposition: Microstructure and mechanical properties," *Materials & Design*, vol. 31, 2010.

[5] B. Baufeld, E. Brandl, and O. V. D. Biest, "Wire based additive layer manufacturing: Comparison of microstructure and mechanical properties of Ti–6Al–4V components fabricated by laser-beam deposition and shaped metal deposition," *Journal of Materials Processing Technology*, vol. 211, no. 6, pp. 1146–1158, 2011.

[6] B. Vrancken, L. Thijs, J.-P. Kruth, and J. V. Humbeeck, "Heat treatment of Ti6Al4V produced by Selective Laser Melting: Microstructure and mechanical properties*," Journal of Alloys and Compounds*, vol. 541, pp. 177–185, 2012.

[7] A. A. Antonysamy and P. B. Prangnell, Microstructure, texture and mechanical property evolution during additive manufacturing of Ti6Al4V alloy for aerospace applications. Manchester, UK: University of Manchester, 2012.

[8] B. E. Carroll, T. A. Palmer, and A. M. Beese, "Anisotropic tensile behavior of Ti–6Al–4V components fabricated with directed energy deposition additive manufacturing," *Acta Materialia*, vol. 87, pp. 309–320, 2015.

[9] P. Kobryn, E. Moore, and S. Semiatin, "The effect of laser power and traverse speed on microstructure, porosity, and build height in laser-deposited Ti-6Al-4V," *Scripta Materialia*, vol. 43, no. 4, pp. 299–305, 2000.

[10] QUADRENNIAL TECHNOLOGY REVIEW: AN ASSESSMENT OF ENERGY TECHNOLOGIES AND RESEARCH OPPORTUNITIES," 2015. [Online]. Available: https://energy.gov/sites/prod/files/2017/03/f34/qtr-2015-chapter6.pdf. [Accessed: 25-Jun-2017].

[11] C. Montgomery, J. C. Beuth, L. Sheridan, and N. Klingbeil, " Process mapping of Inconel 625 in laser powder bed additive manufacturing," *In Solid Freeform Fabrication Symposium*, Austin, TX, 2015, pp. 1195–1204.

[12] F. Nonino and M. K. Niaki, "The impact of additive manufacturing on firms' competitiveness: an empirical investigation," *Production Engineering and Management*, vol. 11, pp. 195–206, 2015.

[13] I. Gibson, D. Rosen, and B. Stucker, Additive Manufacturing Technologies: 3D Printing, Rapid Prototyping, and Direct Digital Manufacturing.: Springer, 2014.

[14] B. Vrancken, Study of Residual Stresses in Selective Laser Melting. 2016.

[15] W. E. Frazier, "Metal Additive Manufacturing: A Review," *Journal of Materials Engineering and Performance*, vol. 23, no. 6, pp. 1917–1928, Aug. 2014.

[16] L. M. Sochalski-Kolbus, E. A. Payzant, P. A. Cornwell, T. R. Watkins, S. S. Babu, R. R. Dehoff, M. Lorenz, O. Ovchinnikova, and C. Duty, "Comparison of

Residual Stresses in Inconel 718 Simple Parts Made by Electron Beam Melting and Direct Laser Metal Sintering," *Metallurgical and Materials Transactions A*, vol. 46, no. 3, pp. 1419–1432, Oct. 2015.

[17] V. Bhavar, P. Kattire, V. Patil, S. Khot, K. Gujar, and R. Singh, "A review on powder bed fusion technology of metal additive manufacturing," *In 4th International Conference and Exhibition on Additive Manufacturing Technologies-AM-2014*, 2014.

[18] H. Gong, K. Rafi, H. Gu, T. Starr, and B. Stucker, "Analysis of defect generation in Ti–6Al–4V parts made using powder bed fusion additive manufacturing processes," *Additive Manufacturing*, vol. 1-4, pp. 87–98, 2014.

[19] A. Vasinonta, J. L. Beuth, and M. L. Griffith, "Process maps for controlling residual stress and melt pool size in laser-based SFF processes," *In Solid Freeform Fabrication Proceedings*, Austin, TX, 2000, pp. 200-208.

[20] S. Bontha, N. W. Klingbeil, P. A. Kobryn, and H. L. Fraser, "Thermal process maps for predicting solidification microstructure in laser fabrication of thin-wall structures," *Journal of Materials Processing Technology*, vol. 178, no. 1-3, pp. 135–142, 2006.

[21] J. Beuth, J. Fox, J. Gockel, C. Montgomery, R. Yang, H. Qiao, and N. Klingbeil, "Process mapping for qualification across multiple direct metal additive manufacturing processes," *In Solid Freeform Fabrication Proceedings*, Austin, TX, 2013, pp. 655-665

[22] J Beuth, N Klingbeil, and J Gockel, "Process Mapping of Cooling Rates and Thermal Gradient," PCT/US2013/055422, August 16, 2013.

[23] J. Gockel and J. Beuth, "Understanding Ti-6Al-4V microstructure control in additive manufacturing via process maps," *Solid Freeform Fabrication Proceedings*, Aug. 2013.

[24] L. Sheridan, An Adapted Approach to Process Mapping across Alloy Systems and Additive Manufacturing Processes. 2016.

[25] M. J. Donachie, Titanium: a technical guide.: ASM International, 2010.

[26] G. Lütjering, "Influence of processing on microstructure and mechanical properties of (α β) titanium alloys," *Materials Science and Engineering: A*, vol. 243, no. 1-2, pp. 32–45, 1998.

[27] M. Simonelli, Microstructure evolution and mechanical properties of selective laser melted Ti-6Al-4V. Great Britain: Loughborough University, 2014.

[28] F. R. Larson and A. Zarkades, Properties of textured titanium alloys. Columbus, OH: Metals and Ceramics Information Center, 1974.

[29] G. A. Sargent, K. T. Kinsel, A. L. Pilchak, A. A. Salem, and S. L. Semiatin, "Variant Selection During Cooling after Beta Annealing of Ti-6Al-4V Ingot Material," *Metallurgical and Materials Transactions A*, vol. 43, no. 10, pp. 3570–3585, 2012.

[30] A. L. Pilchak, W. J. Lu, and J. C. Williams, "Progress in Understanding the Fatigue Behavior of Ti Alloys," *Materials Science Forum*, vol. 710, pp. 85–92, 2012.

[31] A. L. Pilchak, The effect of friction stir processing on the microstructure, mechanical properties and fracture behavior of investment cast Ti-6Al-4V. 2009.

[32] S. L. Semiatin, S. V. Shevchenko, O. M. Ivasishin, M. G. Glavicic, Y. B. Chun, and S. K. Hwang, "Modeling and Simulation of Texture Evolution During the Thermomechanical Processing of Titanium Alloys (PREPRINT)," Jan. 2008.

[33] L. Thijs, F. Verhaeghe, T. Craeghs, J. V. Humbeeck, and J.-P. Kruth, "A study of the microstructural evolution during selective laser melting of Ti–6Al–4V," *Acta Materialia*, vol. 58, no. 9, pp. 3303–3312, 2010.

[34] L. Zhang, D. Klemm, J. Eckert, Y. Hao, and T. Sercombe, "Manufacture by selective laser melting and mechanical behavior of a biomedical Ti–24Nb–4Zr–8Sn alloy," *Scripta Materialia*, vol. 65, no. 1, pp. 21–24, 2011.

[35] M. Simonelli, Y. Tse, and C. Tuck, "Effect of the build orientation on the mechanical properties and fracture modes of SLM Ti–6Al–4V," *Materials Science and Engineering*: A, vol. 616, pp. 1–11, 2014.

[36] T. Vilaro, C. Colin, and J. D. Bartout, "As-Fabricated and Heat-Treated Microstructures of the Ti-6Al-4V Alloy Processed by Selective Laser Melting," *Metallurgical and Materials Transactions A*, vol. 42, no. 10, pp. 3190–3199, 2011.

[37] S. Leuders, M. Thöne, A. Riemer, T. Niendorf, T. Tröster, H. Richard, and H. Maier, "On the mechanical behaviour of titanium alloy TiAl6V4 manufactured by selective laser melting: Fatigue resistance and crack growth performance," *International Journal of Fatigue*, vol. 48, pp. 300–307, 2013.

[38] I. V. Zyl, I. Yadroitsava, and I. Yadroitsev, "Residual Stress In Ti6Al4V Objects Produced By Direct Metal Laser Sintering," *South African Journal of Industrial Engineering*, vol. 27, no. 4, 2016.

[39] N. Rossini, M. Dassisti, K. Benyounis, and A. Olabi, "Methods of measuring residual stresses in components," *Materials & Design*, vol. 35, pp. 572–588, 2012.

[40] "INTEGRATION DE LA NOTION DES," [Online]. Available: https://www.shotpeener.com/library/pdf/1988030.pdf. [Accessed: 12-Aug-2017].

[41] S. A. Martinez, S. Sathish, M. P. Blodgett, S. Namjoshi, and S. Mall, "Residual Stress Relaxation Due to Fretting Fatigue in Shot Peened Surfaces of Ti-6Al-4V," *AIP Conference Proceedings*, 2003.

[42] P. Withers and H. Bhadeshia, "Residual stress. Part 1 – Measurement techniques," *Materials Science and Technology*, vol. 17, no. 4, pp. 355–365, 2001.

[43] P. S. Prevey, X-ray diffraction residual stress techniques.: ASM International, 1986.

[44] P. Mercelis and J. P. Kruth, "Residual stresses in selective laser sintering and selective laser melting," *Rapid Prototyping Journal*, vol. 12, no. 5, pp. 254–265, 2006.

[45] I. Yadroitsev and I. Yadroitsava, "Evaluation of residual stress in stainless steel 316L and Ti6Al4V samples produced by selective laser melting," *Virtual and Physical Prototyping*, vol. 10, no. 2, pp. 67–76, 2015.

[46] "Measurement of Residual Stresses by the Hole-Drilling* Strain Gage Method," 01-Nov-2010. [Online]. Available: http://www.vishaypg.com/docs/11053/tn503.pdf. [Accessed: 23-Sep-2017].

[47] F. A. Kandil, J. D. Lord, A. T. Fry, and P. V. Grant, "A review of residual stress measurement methods. A Guide to Technique Selection," Engineering Industries Directorate of the UK Department of Trade and Industry, rep., 2001.

[48] E. R. Denlinger, J. C. Heigel, P. Michaleris, and T. Palmer, "Effect of inter-layer dwell time on distortion and residual stress in additive manufacturing of titanium and nickel alloys," *Journal of Materials Processing Technology*, vol. 215, pp. 123–131, 2015.

[49] C. Casavola, S. L. Campanelli, and C. Pappalettere, "Experimental analysis of residual stresses in the selective laser melting process," *In Proccedings of the XIth International Congress and Exposition*, 2015.

[50] N. J. Rendler and I. Vigness, "Hole-drilling strain-gage method of measuring residual stresses," *Experimental mechanics*, 1966.

[51] G. S. Schajer, Practical residual stress measurement methods. Chichester: Wiley-Blackwell, 2013.

[52] M. B. Prime, "The contour method: a new approach in experimental mechanics," In *Proceedings of the SEM Annual Conference*, 2009.

[53] A. S. Wu, D. W. Brown, M. Kumar, G. F. Gallegos, and W. E. King, "An Experimental Investigation into Additive Manufacturing-Induced Residual Stresses in 316L Stainless Steel," *Metallurgical and Materials Transactions A*, vol. 45, no. 13, pp. 6260–6270, 2014.

[54] D. J. Greving, E. F. Rybicki, and J. R. Shadley, "Through-thickness residual stress evaluations for several industrial thermal spray coatings using a modified

layer-removal method," *Journal of Thermal Spray Technology*, vol. 3, no. 4, pp. 379–388, 1994.

[55] J. Gockel, J. Beuth, and K. Taminger, "Integrated control of solidification microstructure and melt pool dimensions in electron beam wire feed additive manufacturing of Ti-6Al-4V," *Additive Manufacturing*, vol. 1-4, pp. 119–126, 2014.

[56] B. Vrancken, S. Buls, J.-P. Kruth, and J. V. Humbeeck, "Preheating of Selective Laser Melted Ti6Al4V: Microstructure and Mechanical Properties," *Proceedings of the 13th World Conference on Titanium*, 2015, pp. 1269–1277.

[57] A. Nickel, D. Barnett, and F. Prinz, "Thermal stresses and deposition patterns in layered manufacturing," *Materials Science and Engineering*: A, vol. 317, no. 1-2, pp. 59–64, 2001.

[58] Y. Liu, Y. Yang, and D. Wang, "A study on the residual stress during selective laser melting (SLM) of metallic powder," *The International Journal of Advanced Manufacturing Technology*, vol. 87, no. 1-4, pp. 647–656, 2016.

[59] B. Cheng, S. Shrestha, and Y. K. Chou, "Stress and Deformation Evaluations of Scanning Strategy Effect in Selective Laser Melting," *Volume 3: Joint MSEC-NAMRC Symposia*, 2016.

[60] N. Klingbeil, J. Beuth, R. Chin, and C. Amon, "Residual stress-induced warping in direct metal solid freeform fabrication," *International Journal of Mechanical Sciences*, vol. 44, no. 1, pp. 57–77, 2002.

[61] "EDAX - A leading provider of materials characterization systems," AMETEK EDAX. [Online]. Available: http://www.edax.com/. [Accessed: 01-Dec-2017].

[62] R. B. Ceglias, J. M. Alves, R. A. Botelho, E. D. S. B. Júnior, I. C. D. Santos, Nicki Robbers Darciano Cajueiro De Moraes, R. V. D. Oliveira, S. B. Diniz, and L. P. Brandao, "Residual Stress Evaluation by X-Ray Diffraction and Hole-Drilling in an API 5L X70 Steel Pipe Bent by Hot Induction," *Materials Research*, vol. 19, no. 5, pp. 1176–1179, 2016.